1995A&A...299..523F

Astron. Astrophys. 299, 523–544 (1995)

ASTRONOMY
AND
ASTROPHYSICS

Time-dependent structure and energy transfer in hot star winds

A. Feldmeier

Institut für Astronomie und Astrophysik der Universität, Scheinerstr. 1, D-81679 München, Germany

Received 9 November 1994 / Accepted 3 January 1995

Abstract. We present time-dependent hydrodynamical models of radiation driven hot star winds, which are subject to a strong instability intrinsic to the radiative line force. The calculations are done using a newly developed radiation hydrodynamics code applying the Smooth Source Function method (Owocki 1991) to calculate the radiative acceleration. Assuming spherical symmetry, the wind consists of a sequence of narrow, dense shells, where each shell is bounded by a pair of reverse and forward shocks, in good agreement with comparable models by Owocki (1992). We find frequent encounters of two shells with subsequent merging of the shells into one. For *small* periodic base perturbations, the wind structure is also periodic, without a stochastic component. For *large* base perturbations, on the other hand, a continuous spectrum of wave frequencies is excited in the wind. Furthermore, our models show the shock decay to set in from about 5 stellar radii on.

The major theme of this paper is the *energy transfer* in the wind. Time-dependent supergiant wind models up to now simply assume radiative cooling to be efficient, and hence the shocks to be isothermal. To test this assumption and to calculate the X-ray emission, the energy equation is included in the simulations. A severe numerical shortcoming is then encountered, whereby all radiative cooling zones collapse and the shocks become isothermal again. We propose a new method to hinder this defect. Simulations of dense winds then prove radiative cooling to indeed be efficient *up to* 5 to 7 R_*. Shock temperatures are between 10^6 to 10^7 K, depending on the base perturbation. Beyond these radii, however, the cooling zones of strong shocks become broad and thereby alter the wind structure drastically: all reverse shocks disappear, leaving regions of previously heated gas. This gas cools as it advects to larger radii. Since, moreover, shell-shell collisions only occur up to 6 to 7 R_*, the wind can be divided into two regions: an *inner, active* one with frequent shocks and shell-shell collisions; and an *outer, quiescent* region with "old" hot material, and with no further shell collisions.

Key words: stars: early type – stars: mass-loss – hydrodynamics – instabilities

1. Introduction

The winds of hot, luminous OB stars are driven by the momentum transfer from the star's UV continuum radiation field to metal ions, which is accomplished in numerous line transitions of these ions. Building upon the work by Lucy & Solomon (1970), Castor et al. (1975), and Abbott (1980, 1982), the subsequent inclusion of the finite cone angle effect (Pauldrach et al. 1986; Friend & Abbott 1986), a detailed NLTE treatment of the wind (Pauldrach 1987), radiative transfer allowing for multiple scattering (Puls 1987), and the empirical inclusion of line blocking and shock emission (Pauldrach et al. 1994a) results in stellar wind models which are able to predict the correct mass loss rates and terminal velocities, and to reproduce the complete UV line spectrum (Pauldrach et al. 1994a,b).

The most severe restriction underlying these models is their intrinsic assumption of stationarity. However, a wealth of observational evidence exists for a distinct time-dependency of the winds: 1. In the absorption troughs of ultraviolet P Cygni profiles of strong but unsaturated metal lines one observes the appearance of so-called discrete absorption components (DACs) at 0.3 to 0.5 of the wind's terminal velocity, v_∞. The DACs propagate to near v_∞ on timescales of one to a few days (Prinja & Howarth 1986, 1988; Henrichs 1988; Kaper 1993, and ref. therein). DACs have also been found in the P Cygni profile of the subordinate optical line He I λ5876 of the O supergiants HD 151804 (Fullerton et al. 1992) and HD 152408 (Prinja & Fullerton 1994a,b), starting already at 0.1 v_∞ . Because the recurrence time-scale of the DACs seems to be correlated with the projected rotational velocity of the star (Prinja 1988), a presently favored model of DAC creation is by corotating interaction regions (CIRs; Mullan 1984, 1986). 2. Saturated UV P Cygni profiles often show variability of the blue absorption edge (Henrichs 1991; Kaper 1993), and the appearance of broad and black absorption troughs (Prinja & Howarth 1986; Kaper 1993). The blue edge variability is believed to be caused by (rarefied) high speed material in the wind. The black troughs are thought to be due to a multiple non-monotonic velocity field of the wind (because of, e.g., the occurence of shocks), which in consequence induces a very effective back-scattering of the photopheric radiation (Lucy 1982a, 1983; Puls 1993; Puls et al. 1993b). 3. The X-ray emission from OB stars (EINSTEIN: Harnden et al. 1979;

Seward et al. 1979; Cassinelli & Swank 1983; Chlebowski et al. 1989; ROSAT: Hillier et al. 1993; Cassinelli et al. 1994; Drew et al. 1994) was first proposed to stem from coronal emission regions just above the stellar photosphere (Hearn 1972, 1975; Cassinelli & Olson 1979). These coronal models were subsequently ruled out for mainly two reasons: (i) The deep-seated origin of the X-rays would lead to strong K-shell absorption in the overlying wind material, which is not observed (Cassinelli & Swank 1983; Hillier et al. 1993; Cassinelli et al. 1994). (ii) The green coronal emission line [Fe XIV]5303 Å is not found in high S/N spectra of ζ Pup (Baade & Lucy 1987). The presently favoured model of X-ray emission is therefore by strong shocks in the wind; this is discussed below. 4. A non-thermal component in the radio emission of many OB stars (Abbott et al. 1981, 1984b; Bieging et al. 1989) is interpreted to be synchrotron radiation by shock-accelerated particles (White 1985). This interpretation is supported by the correlation found between X-ray emission and non-thermal radio emission (Chlebowski 1989). 5. With mass loss rates inferred from radio data, the observed thermal IR emission of winds is often too large when a smooth, stationary wind model with a $\beta < 1$ velocity law is applied (Abbott et al. 1984a). Because the free-free IR emission is a density-squared process, this enhanced flux can be explained by clumpiness of the winds in the region of the IR formation (Abbott el al. 1984a; Lamers & Waters 1984; Puls et al. 1993a). Clumpiness close to the stellar photosphere may also influence the formation of optical transitions such as Hα (Ebbets 1982; Wolf et al. 1994; Kaufer et al. 1994; Puls et al. 1995) or He I λ5876 (Prinja & Fullerton 1994a,b). 6. Finally, recent observations by the Gamma Ray Observatory of a WR star (White 1994) suggest that the postulated γ-ray emission from hot star winds (White & Chen 1992a,b) has readily been detected. The γ-rays should stem from pion decays, where the pions in turn are produced by collisions of thermal ions with protons Fermi-accelerated in shocks. The energies of these γ-rays are ≈ 5 decades higher than observed X-ray energies.

The major cause of wind structure is thought to be the strong hydrodynamical instability intrinsic to the line driving of the wind. (Possible exceptions to this are the DACs, the appearance of which might be connected to photospheric perturbations, where the latter induce *stable*, large scale structures propagating through the wind.) Milne (1926) proposed in essence this instability (or runaway) mechanism for the first time, for single ions in a static atmosphere. However, these runaway ions would lose their excess energy by Coulomb collisions with surrounding ions. Contrary to this, the wind instability proposed by Lucy & Solomon (1970) does not apply to single ions, but instead to hydrodynamical fluid particles. The mechanism of this instability is discussed extensively by Owocki & Rybicki (1984; hereafter OR) and by Rybicki (1987). OR succeeded in the unification (the so-called "bridging law") of the disparate results of MacGregor et al. (1979) and Carlberg (1980), who proposed a strong wind instability, and Abbott (1980), who proposed stability instead. Following OR, unstable growth should only occur for optically thin perturbations of optically thick lines, whereas optically thick perturbations should be stable. A further twist came into the stability vs. instability discussion by Lucy's (1984) discovery of the *line drag effect*. This effect stabilizes the flow due to the enhanced back*scattered* flux from larger radii which is experienced by a particle with outward directed velocity perturbation. This leads to zero growth rates very close to the star; but already within one stellar radius (Owocki & Rybicki 1985) the growth rate has reached again half the value of the pure absorption case considered by Carlberg (1980) and OR.

Since the typical growth rate within a characteristic wind flow time is of the order of 100 e-folds, the growth of perturbations will quickly reach the non-linear regime. Phenomenological models of the fully developed wind structure were proposed by Lucy & White (1980), Lucy (1982b), and MacFarlane & Cassinelli (1989), and are discussed below. The first consistent numerical simulations of the unstable growth were presented by Owocki et al. (1988; hereafter OCR). The three central assumptions underlying their work are: (i) one-dimensional spherical symmetry of the flow; (ii) isothermality; and (iii) pure photon absorption in spectral lines (no re-emission). The latter assumption has been dropped in subsequent work (Owocki 1991, 1995) by the approximate inclusion of line scattering using the so-called smooth source function method (SSF). The principal wind structures of pure absorption models and SSF models (but not the location of onset of the structure) are identical: the stationary wind at time $t = 0$ is transformed into an outward migrating sequence of very narrow and dense shells, which are enclosed by a strong reverse shock on the starward side and a weaker forward shock on the outer side.

The central part of the present paper deals with relaxing the above assumption of isothermality, (ii). There are mainly three reasons for doing so: 1. To calculate the X-ray emission from a time-dependent wind model one needs to know the temperature distribution of the wind material. 2. Isothermality should be a good approximation only for *dense* winds with efficient radiative cooling, where cooling zones are short enough to have no influence on the wind dynamics. On the other hand, radiative energy losses are small in the thin winds of B near main sequence stars (Lucy & White 1980), and also in rarefied regions of OB supergiant winds. Besides at large distances from the star, such regions possibly also exist at small radii due to the extreme dilution of the intershell medium in time-dependent wind models. 3. The EUV radiation of shock heated matter has an important influence on the ionization balance in the wind (Pauldrach et al. 1994a,b).

The energy transfer and X-ray emission is also the concern of most phenomenological models of the wind structure so far: Lucy & White (1980) proposed the X-rays to originate from bow shocks surrounding radiatively driven blobs ploughing through rarefied, shadowed, and therefore not radiatively driven wind material. The energy dissipation due to the friction between these two components is accomplished in the shock fronts. In this model, X-rays from blobs lying close to the star should experience strong K-shell absorption in the overlying wind material, which is not observed (Cassinelli & Swank 1983). Lucy (1982b) simplified the 2-D blob model to a 1-D model of a sawtooth like sequence of forward shocks. Within this model, the

1995A&A...299..523F

mutual shadowing of shocks ("blobs") is included. Because of this shadowing, the distance between shocks is larger; therefore shocks can exist up to larger radii and K-shell absorption has almost no significance, in accord with observations. The shortcoming of this model is that the resulting X-ray spectrum is too soft and too weak (Lucy 1982b; Cassinelli & Swank 1983). Finally, MacFarlane & Cassinelli (1989) proposed a model for the X-ray emission from the main-sequence B0 star τ Sco, which is able to reproduce the observed EINSTEIN data well. In this model, the propagation of a *single* shell through the wind is followed. The radiative line force is assumed to be stable, and consequently the shell does not evolve from an initially small perturbation, but instead is created by a strong, arbitrary perturbation of the boundary (MacFarlane & Cassinelli 1989) or the initial (Cooper & Owocki 1992) conditions of the wind. The importance of single, strong shocks for the X-ray emission from winds has already been noted by Lucy (1982b) (cf. also Cassinelli et al. 1994).

The first hydrodynamical wind models including the *energy* transfer of the unstable growth of initially small perturbations were presented by Cooper & Owocki (1992). These authors encounter a numerical shortcoming due to the radiative cooling of the gas: cooling zones behind strong shocks are not resolved, instead the shocks become isothermal again. This is the case even on a very fine spatial grid. Because of this problem, Cooper & Owocki (1992) neglected completely the radiative cooling in *thin* winds. The X-ray flux from these models was found to be typically a factor of 10 smaller than the observed flux. Cooper & Owocki (1994) therefore concluded that a large fraction of the (thin) wind material above a certain radius is heated to X-ray temperatures, which was also suggested by Cassinelli et al. (1994). For dense winds with their efficient cooling, on the other hand, Cooper (1994) and Cooper & Owocki (1994) suppose the cooling zones behind shocks to be steady (i.e., the cooling time is much shorter than the time-scale for changes in shock parameters). The X-ray spectrum from the shocks of an *isothermal* wind model is then found by using a tabulation of the emission as function of post-shock temperature. Contrary to the case of thin winds, the calculated X-ray flux from dense winds is found to be typically a factor of 10 *larger* than the observed flux.

In the present paper, we concentrate on the *consistent* inclusion of the energy transfer in time-dependent hydrodynamical wind simulations. To this aim, the origin of the above collapse of the radiative cooling zones is revealed and a method proposed to hinder it. Besides the assumption of 1-D spherical symmetry still remaining, the further main restrictions of our calculations are: 1. Only dense winds of O supergiants are considered, leaving the study of thin winds of B main sequence stars to future work. 2. Only the wind *dynamics* is considered. The calculation of X-ray emission from the models and comparison with ROSAT observations will be given in a follow-up paper.

The rest of this paper is organized as follows: Sect. 2 describes the numerical technique applied in calculating time-dependent wind models. In Sect. 3, an *isothermal* model for a supergiant wind is presented and compared with results by Owocki (1992, 1994). Section 4 discusses the numerical problem of the collapse of the radiative cooling zones behind strong shocks by means of a simple test flow problem and proposes a method to hinder this collapse. In Sect. 5, wind models including the energy transfer are examined. Section 6 gives a summary of results.

2. Technique

2.1. The hydrodynamical equations

The radiation hydrodynamical wind equations are, assuming an inviscid, one-component flow,

$$\frac{\partial \rho}{\partial t} + \mathrm{div}(\rho\,\mathbf{v}) = 0, \tag{1}$$

$$\frac{\partial (\rho \mathbf{v})}{\partial t} + \mathrm{div}(\rho \mathbf{v} \otimes \mathbf{v}) = -\mathrm{grad}\, p - \rho\, \mathbf{g}_{\mathrm{grav}} + \rho\, \mathbf{g}_{\mathrm{line}}, \tag{2}$$

$$\frac{\partial e}{\partial t} + \mathrm{div}(e\,\mathbf{v}) = -p\,\mathrm{div}\,\mathbf{v} - \Lambda. \tag{3}$$

The thermal energy density, e, of an ideal gas is $e = p/(\gamma - 1)$, where $\gamma = 5/3$ is assumed in the following.

The expressions for the radiative line acceleration $\mathbf{g}_{\mathrm{line}}$ and for the radiative cooling function Λ ($\sim \rho^2$) are given below. The temperature dependence of both the line force and the radiative cooling rate should in principle be found from a time-dependent, non-LTE treatment of the wind plasma. At least the first of these will likely remain beyond the capacity of computers for the foreseeable future. Here we simply parameterize the temperature dependence as found from stationary equilibrium calculations by Raymond et al. (1976) [cooling function] and MacGregor et al. (1979) [radiative force].

In the following, we will restrict ourselves to 1-D spherical symmetry: the calculation of the radiative line force in 2 or more dimensions is beyond current computer capabilities. Physical justification for assuming a spherically symmetric flow comes from the fact that the unstable growth of waves with "lateral velocity polarization" is damped because of Lucy's (1984) line drag effect (Rybicki et al. 1990). As long as the amplitude of photospheric perturbations, which are *assumed* in the present paper to seed the wind structure, has no strong dependence on latitude or azimuth, one then would expect the appearance of shell-like structures in the wind. In more realistic 2-D and 3-D models, however, even weak azimuthal perturbations could grow nonlinearly and break the shells into clumps due to instabilities of the Rayleigh-Taylor or the Kelvin-Helmholtz type (cf. Chandrasekhar 1961).

2.2. The hydrodynamical scheme

Equations (1) to (3) are discretized using an operator-splitting time-explicit, finite differences Eulerian scheme on staggered grids (cf. Reile & Gehren 1991a,b). The advection terms in integral form are solved on the control volumes of these grids (see, e.g., Roache 1982). This automatically ensures the correct jump conditions at shocks (and the correct shock positions), *if* the hydrodynamical equations are in conservative form. However, Eq. (3) is the thermal (not the total) energy equation, which is not conservative. We will return to this point in the next section. The advection fluxes are calculated using van Leer's (1977) monotonic interpolation. For the calculations in the present paper we applied the *consistent advection* scheme of Norman et al. (1980), since otherwise spurious spikes would show up in the velocity field (Owocki 1991).

The consistent advection scheme after Norman et al. (1980; see also Norman & Winkler 1986, and Stone & Norman 1992) may be described as follows. Let $\mathbb{F}$ be a conserved quantity like mass, momentum (in the absence of forces), or total energy; let $f = \mathrm{d}\mathbb{F}/\mathrm{d}V$ (with volume V) be the $\mathbb{F}$-density, and let $\mathbf{F}(f) = \hat{f}\,\mathbf{v}$ be the corresponding flux vector. The circumflex in the last expression indicates that the f value is *interpolated*, e.g., using either the donor cell scheme, the van Leer scheme, or the piecewise parabolic scheme (Colella & Woodward 1984). This is necessary since f and $\mathbf{F}$ are defined at different locations on the staggered grids, i.e., f at volume centers and $\mathbf{F}$ on volume boundaries. Consistent advection now means the replacement of the above ("standard") flux expression by

$$\mathbf{F}(f) = \hat{f}\,\mathbf{v} \rightarrow \widehat{f/\rho}\,\mathbf{F}(\rho), \tag{4}$$

with mass flux $\mathbf{F}(\rho) = \hat{\rho}\,\mathbf{v}$.

Finally, the *pressure terms* in the momentum and the energy equation, as well as g_{grav} and g_{line} in the momentum equation, are discretized in a straightforward manner. – The *boundary conditions* at R_{min} and R_{max} are fixed via Riemann invariants. R_{min} is the stellar photosphere. Here, an isothermal exponential density stratification through which a sound wave propagates into the wind is assumed as boundary condition. At R_{max}, Hedstrom's (1979) nonreflecting boundary conditions are applied using the formalism described by Thompson (1987, 1990).

2.3. The energy equation

In supergiant winds with flow speeds of a few thousand km/s and thermal speeds of about 3 km/s for ions like Fe and Ni, the ratio of the thermal energy of these ions to their macroscopic flow energy is of the order of 10^{-6}. However, behind strong shock fronts this ratio can approach unity. Hence, the thermal energy is an ill-conditioned part of the total kinetic energy of the wind plasma. For this reason we solve the *thermal* energy equation instead of the conservative *total* energy equation.

To ensure correct shock jumps, *artificial viscosity* is used in the tensor formulation of Schulz (1964) and Winkler & Norman (1986). In this formulation, only the viscosity *coefficient* is "artificial", in that it depends on the velocity gradient.

To solve for the adiabatic part of the energy equation plus the contribution from artificial viscosity (but without the radiative cooling), the operator splitting scheme of Norman & Winkler (1986) is used. The central part of this scheme is an implicit expression for the pressure, which should "optimize" energy conservation. In contrast to this, the scheme proposed by Hawley et al. (1984) only ensures positivity of the thermal energy. After this adiabatic + viscous step, all variables are updated and the radiative cooling rate is calculated. Other possible operator splitting schemes include: (i) the one after Różyczka (1985), where adiabatic terms and radiative cooling terms are mixed; and (ii) the scheme after Mair et al. (1988), where the radiative cooling is calculated in two half-steps, i.e., before and after the solution of the adiabatic part of the energy equation. We use the simple scheme described above because it makes a clear distinction between adiabatic and non-adiabatic terms, and thereby allows a simple analysis of the numerical behaviour of the radiative cooling. Assuming the cooling function to be of power law form, $\Lambda = A\rho^2 T^\alpha$, the equation for radiative cooling in this scheme is (cf. Eq. (3)),

$$\frac{\mathrm{d}T}{\mathrm{d}t} = -BT^\alpha, \tag{5}$$

with constant B,

$$B = \frac{\mu(\gamma - 1)}{k} A\rho. \tag{6}$$

μ and k are the mean molecular weight and the Boltzmann constant, respectively. Note that ρ in Eq. (6) is a constant, since the density is updated only once during the numerical time step, in solving the continuity equation. The solution of the differential equation (5), for $\alpha \neq 1$, is

$$T_{n+1} = T_n \left[1 - (1 - \alpha) \frac{\Delta t}{\tau_{\mathrm{c},n}} \right]^{\frac{1}{1-\alpha}}, \tag{7}$$

with the *cooling time* (at time step n)

$$\tau_{\mathrm{c},n} = \frac{T_n^{1-\alpha}}{B}. \tag{8}$$

From the requirement that the term in square brackets in (7) is *positive*, one finds the time step limitation

$$\Delta t \leq \frac{\tau_{\mathrm{c},n}}{1 - \alpha} \qquad \text{for} \qquad \alpha < 1. \tag{9}$$

For $\alpha \geq 1$, on the other hand, there is no limitation on the time step.

For time-explicit differencing of (5) (instead of solving the differential equation directly), one finds the time step limitation, again requiring positive temperatures, $\Delta t \leq \tau_{\mathrm{c},n}$. For the semi-implicit and fully implicit differencing of (5) (see Roache 1982) the time step limitation has to be calculated separately for each value of α. For the case $\alpha = -1/2$, which is of interest here (see below), one finds $\Delta t \leq \frac{4}{3\sqrt{3}}\tau_{\mathrm{c},n}$ (semi-implicit), and $\Delta t \leq \frac{2}{3\sqrt{3}}\tau_{\mathrm{c},n}$ (fully implicit).

These time step limitations from the demand for positive temperatures are to be distinguished from time step limitations from numerical stability. A linear stability analysis of the exact solution (7) of (5), as well as of the time explicit and time implicit versions of (5) all lead to the following result: For $\alpha < 0$, temperature perturbations always *grow* in course of time, $|\Delta T_{n+1}/\Delta T_n| > 1$, even for an arbitrary short time step

Δt . However, this does not indicate numerical instability, but instead is a simple manifestation of Field's (1965) cooling runaway: material which becomes cooler than its surroundings will usually enlarge this temperature difference in time, since radiative cooling proceeds more efficiently for cooler material. Field's isochoric instability criterion (the density is constant in (5)) is precisely $\alpha < 0$, see his Eq. (4a). It therefore appears to us that for $\alpha < 0$, no time step limitation can be drawn from a linear stability analysis of the radiative cooling equation.

For the calculations in this paper, we have chosen a time step

$$\Delta t = \min\left(\Delta t_{\rm CFL},\ \Delta t_{\rm vis},\ \Delta t_{\rm cool}\right), \tag{10}$$

where

$$\begin{aligned}
\Delta t_{\rm CFL} &= \sigma \min_{\rm (grid)} \frac{\Delta r}{a + |v|}, \qquad \sigma = 0.5, \\
\Delta t_{\rm vis} &= \min_{\rm (grid)} \frac{(\Delta r)^2}{2\nu}, \quad \nu = -(b\Delta r)^2 \min(0, {\rm div}\, v), \quad b = 1, \\
\Delta t_{\rm cool} &= \max\left(\frac{1}{3} \min_{\rm (grid)} \tau_{\rm c},\ \ \tau_{\rm z}\right).
\end{aligned} \tag{11}$$

Here, $\Delta t_{\rm CFL}$ is the Courant et al. (1928) time step, with a the sound speed. $\Delta t_{\rm vis}$ is the time step limitation from linear viscosity (cf. Roache 1982), which is also applied to (nonlinear) artificial viscosity (Stone & Norman 1992). $\tau_{\rm c}/3$ in the radiative cooling time step $\Delta t_{\rm cool}$ corresponds to half the maximum allowed time step (9) for $\alpha = -1/2$. $\tau_{\rm z}$ is a lower cutoff time to prevent the resolution of prohibitively short cooling intervals. Under very general assumptions one can easily show that for a post-shock cooling time $\tau_{\rm c} < \Delta t_{\rm CFL}$ the corresponding cooling zone behind the shock front cannot be resolved since it is shorter than the grid distance. Therefore, it should be safe to assume $\tau_{\rm z} \equiv \Delta t_{\rm CFL}$, i.e., to neglect the limitation on the time step from radiative cooling altogether. Proceeding in this way, negative temperatures occur frequently; however, they can simply be replaced by some arbitrary *floor value* for the temperature. Test calculations we have performed for the extreme cases $\tau_{\rm z} = 0$ and $\tau_{\rm z} = \Delta t_{\rm CFL}$ indeed gave essentially the same results.

2.4. The radiative line force

The radiative acceleration in the radial direction (spherical symmetry is assumed) in an isolated spectral line of frequency $\nu_{\rm L}$ and constant mass absorption coefficient $\kappa_{\rm L}$ is,

$$\begin{aligned}
g_{\kappa_{\rm L},\nu_{\rm L}}(r) = \frac{4\pi}{c^2}\kappa_{\rm L}\nu_{\rm L}v_{\rm th} \Bigg\{ & \frac{1}{2} I_{\nu_{\rm L}}(R_*) \int_0^1 {\rm d}\mu\, \mu\, D(\mu) \ \times \\
& \int_{-\infty}^{\infty} {\rm d}x\, \phi\left(x - \frac{\mu v(r)}{v_{\rm th}}\right) P(x) e^{-(\tau_{\rm L}(r,\mu,x)-\tau_0)} \\
& + \frac{1}{2}\int_{-1}^{1} {\rm d}\mu\, \mu \int_{-\infty}^{\infty} {\rm d}x\, \phi\left(x - \frac{\mu v(r)}{v_{\rm th}}\right) \ \times \\
& \int_{\tau_0}^{\tau_{\rm L}(r,\mu,x)} {\rm d}\tau'\, S_{\nu_{\rm L}}(r'(\tau'))\, e^{-|\tau_{\rm L}(r,\mu,x)-\tau'|} \Bigg\}.
\end{aligned} \tag{12}$$

Here, x is the normalized frequency variable of the line (assuming pure Doppler broadening with normalized profile function ϕ), $x_{\nu_{\rm L}} = \nu - \nu_{\rm L}/\Delta\nu_D$, where $\Delta\nu_D = \nu_{\rm L}v_{\rm th}/c$. The mass absorption coefficient $\kappa_{\rm L}$ (in cm^2/g) is taken to be constant, which is a good approximation for resonance lines. A core-halo approximation (optically thin continuum) has been applied in the above expression, where the function $D(\mu)$ describes the angle dependence of the photospheric intensity, and $P(x)$ is the photospheric profile of the line (the transmission of a Schuster-Schwarzschild layer is proposed by OCR). τ_0 is the optical depth at $r = R_*$ or $r \equiv \infty$, depending on whether the ray hits the stellar core or not.

For simplicity, it is assumed that the line corresponds to a *singlet* transition, and that the line is *isolated*, i.e., no line overlap effects are considered. For a discussion of the latter, see Owocki & Rybicki (1985), Puls (1987), and Puls et al. (1993b).

The total radiative force from a large number of wind driving lines is found by integration of the single-line force over the truncated CAK line distribution function (cf. OCR),

$$\begin{aligned}
g_{\rm line}(r) &= \int_0^{\infty} {\rm d}\kappa \int_0^{\infty} {\rm d}\nu\ N(\kappa,\nu)\ g_{\kappa,\nu}(r), \\
N(\kappa,\nu) &= \frac{1}{\nu}\,\frac{1}{\kappa_0}\left(\frac{\kappa_0}{\kappa}\right)^{2-\alpha} e^{-\kappa/\kappa_{\rm max}},
\end{aligned} \tag{13}$$

where $\alpha < 1$. The cutoff $\kappa_{\rm max} < \kappa_0$ is introduced to suppress unstable growth on length scales shorter than the grid resolution, which is due to (very) strong lines.

The idea of the *Smooth Source Function* method (Owocki 1991, 1995) is to assume that the line source function $S_{\nu_{\rm L}}(r)$ is "insensitive to the details of dynamical variations" (Owocki 1991), so that one may adopt the source function for a *stationary* flow. However, for a non-monotonic velocity field (due to, e.g., shocks), radiative couplings occur between different locations in the wind. In case of spatially *separated*, coupled resonance zones (i.e., if there exists a location r in between two coupled regions R_1 and R_2, such that $|(\mu v)_r - (\mu v)_{R_{1,2}}| > n v_{\rm th}$, with $n = O(1)$), an iteration procedure within the generalized Sobolev approximation of Rybicki & Hummer (1978) could be used to calculate the source function. This is done in Puls et al. (1993b) for *line formation* calculations in structured winds, and could be applied in future hydrodynamical simulations. In the present paper, only a *local* source function is used.

In both cases of optically thin and thick lines, simple analytical expressions can be given for the source function in local Sobolev approximation. For reasons of computing time, the calculations in the present paper are done using an opacity independent source function, which is taken here to be the source function for an optically thin line only, corresponding to pure geometric dilution of the radiation field. Calculations using the source function for an optically thick line can be found in Puls et al. (1994). Wind models using a source function which fixes the growth rate to the value predicted from the *linear* stability analysis of Owocki & Rybicki (1985) are discussed by Owocki (1994).

Again for reasons of computing time, the angle integration in (12) is replaced by a one-ray quadrature (Owocki 1991). The different domains of integration over solid angle in the direct and diffuse terms are accounted for by a scaling factor $(r/R_*)^2$. Using the Stefan-Boltzmann law, neglecting limb-darkening, and integrating over the truncated line distribution function one finds (see Owocki 1991 or Feldmeier 1993 for some missing steps),

$$\begin{aligned} g_{\rm line}(r) = {} & \frac{\sigma T_{\rm eff}^4}{c}\Gamma(\alpha)\left(\frac{\kappa_0 v_{\rm th}}{c}\right)^{1-\alpha}\left(\frac{v_{\rm th}}{c}\right)^{\alpha}\frac{R_*^2}{r^2} \times \\ & \left\{\int_{-\infty}^{\infty} {\rm d}x\,\phi\left(x-\frac{\mu v(r)}{v_{\rm th}}\right)\eta_+^{-\alpha}(r,\mu,x)\right. \\ & +\frac{S(r)r^2}{I_* R_*^2}\int_{-\infty}^{\infty} {\rm d}x\,\phi\left(x-\frac{\mu v(r)}{v_{\rm th}}\right) \times \\ & \left.\left[\eta_-^{-\alpha}(r,\mu,x)-\eta_+^{-\alpha}(r,\mu,x)\right]\right\}. \end{aligned} \tag{14}$$

Here, Γ is the Gamma function, and $S \equiv \int {\rm d}\nu S_\nu$, $I_* \equiv \int {\rm d}\nu I_{*,\nu}$. In addition, $S_{\rm thin}(r)/I_* = W$, with $W = \frac{1}{2}(1-\mu_*)$ the dilution factor, and $\mu_* = \sqrt{1-(R_*/r)^2}$. The functions $\eta_\pm$ are given by:

$$\begin{aligned} \eta_+(r,\mu,x) &= {\kappa_{\rm L}}^{-1}\tau_{\rm L}(r,\mu,x)-\eta_0(x)+\kappa_{\rm max}^{-1}+\sigma_e^{-1}\phi(x), \\ \eta_-(r,\mu,x) &= \eta_R(x)-{\kappa_{\rm L}}^{-1}\tau_{\rm L}(r,\mu,x)+\kappa_{\rm max}^{-1}. \end{aligned} \tag{15}$$

The term $\phi(x)/\sigma_e$ (with σ_e the Thomson scattering coefficient) in the expression for η_+ arises from the Schuster-Schwarzschild photospheric layer (cf. OCR). The boundary conditions used are $\eta_0 \equiv 0$ at the stellar core and $\eta_R(x) = R\,\rho(R)\,\phi(x-\mu_R v_R)$ at the maximum radius R, see Owocki (1991).

In the expressions for the line force up to now the wind was assumed to be isothermal. The *temperature dependence* of the force from an optically thin line can be written in the form $g_{\rm thin}(r,T(r)) = F(T) g_{\rm thin}(r,T_{\rm eff})$. The function F then enters the total force from *all* contributing lines (optically thin and thick) in two ways: (i) as a multiplicative factor, as just defined; and (ii) in the expression for the optical depth, since hot material is more transparent ($F < 1$) than cold material. Finally, one has to account for the temperature dependence of $v_{\rm th}$ in the profile function. This latter step is accomplished in (12) by noting that both the products $\kappa v_{\rm th}$ and $x v_{\rm th}$ are independent of temperature, and therefore can be replaced by the corresponding products at $T_{\rm eff}$.

For the function F we use the fit by MacFarlane & Cassinelli (1989) to the numerical results of MacGregor et al. (1979). We then have $F = 1$ below a certain cutoff temperature $T_{\rm cut}$. Above $T_{\rm cut}$, F drops exponentially.

2.5. *The radiative cooling function*

The radiative cooling function from Raymond et al. (1976) for an optically thin gas can be approximated in the temperature range $10^5\,{\rm K} < T < 10^7\,{\rm K}$ by a power law ($N_{\rm e}$ and $N_{\rm H}$ being the electron and hydrogen particle densities, respectively),

$$\Lambda = N_{\rm e} N_{\rm H} A_{\rm R} T^{\alpha}, \tag{16}$$

where

$$\alpha = -\frac{1}{2}, \qquad \text{and} \qquad A_{\rm R} = 1.64\;10^{-19}\,{\rm erg\,cm^3\,K^{\frac{1}{2}}\,s^{-1}}. \tag{17}$$

A better fit to the Raymond et al. cooling function is achieved by assuming distinct power laws in 5 temperature sub-intervals (Rosner et al. 1978). However, in the present framework we use the simple fit (16), (17) only. The reason is that, depending on the value of α, two different *thermal instabilities* possibly complicate the wind dynamics: (i) Field's (1965) local runaway instability; and (ii) the global oscillatory instability of Langer et al. (1981, 1982). Therefore, using only one value for α certainly helps to keep the calculations more lucid, and at the same time should be a sufficiently good approximation for our present purpose, namely to investigate the principles of the energy transfer in the winds.

2.6. *The wind model*

Since ζ Puppies is a well-studied O supergiant, stellar parameters close to the ones of ζ Pup are used in the following calculations. Table 1 lists the stellar and wind parameters.

The line force instability has a significant growth rate only for velocity perturbations with a wavelength shorter than $\frac{1}{3}$ to $\frac{1}{2}$ the Sobolev length $L_{\rm Sob} = v_{\rm th}/({\rm d}v_{\rm stat}/{\rm d}r)$ of the stationary wind (OR). The numerical grid therefore has to be fine enough to resolve these very short length scales. We use 3 000 logarithmically spaced grid points out to $10\,R_*$, i.e., $\Delta r/r = 7.68\;10^{-4}$. The worst resolution of the Sobolev zones occurs in the region of maximum velocity gradients, i.e., close to the sonic point, and is $\min(L_{\rm Sob,stat.}/\Delta r) \lesssim 3$.

The formation of structure in the wind is triggered by a photospheric sound wave which propagates out into the wind, acting as a seed perturbation there. Other photospheric triggering mechanisms, especially non-radial pulsations (see Baade 1991; Gies 1991) and strange mode oscillations (see Gautschy & Glatzel 1990; Kiriakidis et al. 1993), will be studied in future work. The dispersion relation for isothermal sound waves of period P in an isothermal atmosphere of scale height H is (Lamb 1932),

$$\lambda = \frac{\lambda_0}{\sqrt{1-(\lambda_0/4\pi H)^2}}, \qquad \text{with} \qquad \lambda_0 = aP. \tag{18}$$

a is the isothermal sound speed in the limit of $\Lambda \ll H$. Even for sound waves with a wavelength somewhat larger than H, the *linear* dispersion relation $\lambda = aP$ still holds approximately: In our model, $\lambda/H = 5.2$, but still $\lambda/\lambda_0 = 1.1$. The *acoustic cutoff*

Table 1. Stellar and wind parameters. The stellar parameters are taken from Kudritzki et al. (1983).

Parameter	Symbol	Value
Mass	M	$42\,M_\odot$
Temperature	$T_{\rm eff}$	42 000 K
Radius	R_*	$19\,R_\odot$
Luminosity	L	$1.0\,10^6 L_\odot$
Helium fraction	$Y = N_{\rm He}/N_{\rm H}$	0.16
Ionization degree	$I_{\rm H};\ I_{\rm He}$	1; 2
Thomson coefficient	σ_e	$0.32\,{\rm cm}^2\,{\rm g}^{-1}$
Eddington factor	Γ	0.59
Scale height (isoth.)	H	$3.1\,10^{-3}\,R_*$
CAK exponent	α	0.72
Line force constant	$\kappa_0\, v_{\rm th}/c$	$1800\,{\rm cm}^2\,{\rm g}^{-1}$
Line strength cutoff	$\kappa_{\rm max}/\kappa_0$	10^{-3}
Mass loss rate	$\dot M$	$3\ 10^{-6}\,M_\odot\,{\rm yr}^{-1}$
Escape velocity	$v_{\rm esc}$	$580\ {\rm km\,s}^{-1}$
Terminal speed	v_∞	$2\,000\ {\rm km\,s}^{-1}$
Sound speed (isoth.)	$a_{\rm iso}$	$23\ {\rm km\,s}^{-1}$
Thermal speed	$v_{\rm th}$	$0.3\,a_{\rm iso}$
Sound wave: Period	P	5 000 s
——Amplitude at R_*	$A = \delta\rho/\rho$	0.01
——Wavelength	λ	$8.7\ 10^{-3}\,R_*$

period, on the other hand, at which the wavelength of a sound wave becomes infinite (i.e., the denominator in (18) becomes zero), is $P_{\rm cut} = 6.2$ h for the stellar parameters of Table 1.

3. Isothermal wind models

In this section, the energy equation is trivially solved by setting $p = a^2\rho$. This corresponds to the calculations by OCR and Owocki (1992, 1994). The reason to assume supergiant winds to be dynamically isothermal is their high density, which implies that radiative cooling should be efficient enough to keep cooling lengths short compared with dynamical length scales.

Figs. 1 shows the wind structure 10 days after model start. We have followed the calculation for this long time interval for two reasons: (i) To make sure that the wind has completely settled in its response to the photospheric sound wave. As will be seen below, this may sometimes take $\approx$ 1 week. (ii) To permit us to perform a Fourier transformation of the wind velocity (at fixed locations r) as a function of time.

As in the models by OCR and Owocki (1992, 1994), the wind in Fig. 1 consists of a sequence of very narrow, very dense shells. The shells are enclosed by a reverse shock on the starward facing side. On the outward side, it can actually not be decided from the rather poor resolution whether the shells are bounded by a forward shock or by a continuous, forward-facing compression wave (as opposed to a rarefaction wave; see Courant & Friedrichs 1948, Chap. III). Density contrasts of a few thousand occur at the reverse shocks, corresponding to Mach numbers of 30 and more. Because of these large compression ratios, the dense shells in Fig. 1 are very narrow and the reverse and forward shocks that enclose a shell propagate at about the same speed (cf. Sturrock & Spreiter 1965). The forward (reverse) shocks are faster (slower) in any reference frame than both the in- and outflowing material. Because of this, every wind particle passes at most through one shock; or, stated differently, a particle cannot leave a shell once it is in it.

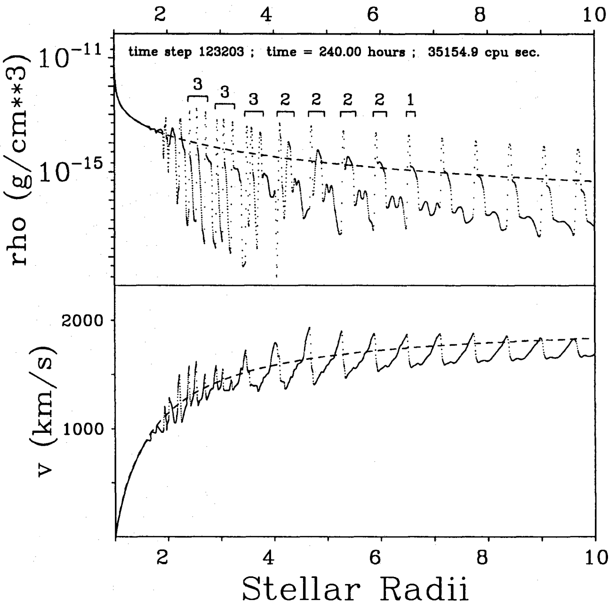

Fig. 1. Isothermal wind 10 days after model start. The values of ρ and v at each grid point are plotted. Dashed line: Stationary start model

It is interesting that the wind structure in Fig. 1, which results from the unstable amplification of the periodic base perturbations, appears itself to be quite stable. This is despite the fact that the material in front of the reverse shocks (i.e., on their left side) shows large velocity gradients, and thus might be expected to be subject to further, smaller scale instability. However, this material is strongly rarefied, so that no optically thick lines are present, which is the other prerequisite for unstable growth to occur. Inside the shells, on the other hand, the material is extremely dense, but here the velocity gradients are negative, which means these regions are stable as well. The regions in front of the forward shocks (i.e., on the right) are stable because of a combination of small velocity gradients (due to shadowing by material at smaller radii) and the depletion of the pre-shock gas. – In effect, the unstable amplification of the driving perturbations suppresses the formation of structure on other scales.

A striking fact about the wind model of Fig. 1 is its strong periodicity at radii larger than 4 R_*. The cause for the *seemingly* chaotic structure in Fig. 1 up to about 4 R_* is the creation of the shells in triples per period of the photospheric sound wave, with subsequent collisions among their members. n-tuples are indicated in the density run of Fig. 1 by $\overset{n}{\sqcap}$. The triple-wise creation of shells and their collisions thereafter are also clearly seen in

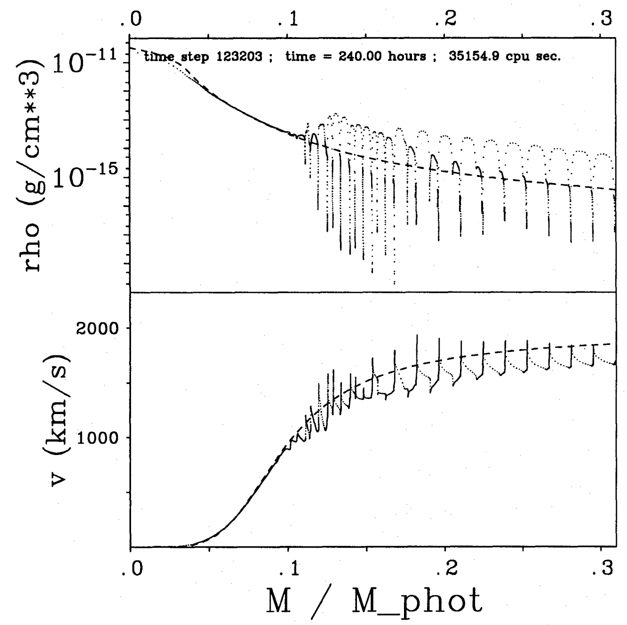

Fig. 2. Wind structure from Figs. 1, plotted against mass coordinate

Fig. 9 for a wind model including the energy transfer, and will be discussed further in Sect. 5.

From about 5 R_* on, the shocks which enclose the shells become weaker with increasing distance from the star. The reason for this is twofold: (i) The instability is strong only close to the star, where the velocity gradient is large. (ii) Shocks far out in the wind are shadowed by material close to the star. This shock decay is not present in models by Owocki and Cooper, where instead the shock amplitude stays almost constant as function of radius. The observable X-ray emission should depend sensitively on the maximum radius for formation of strong shocks. As found by Hillier et al. (1993) for ζ Pup, X-rays with energies below 1 keV originate from radii (much) larger than $10\,R_*$. Detailed modeling of the X-ray emission from time-dependent winds has to clarify the extent to which weak shocks (still present at large radii) are able to produce the observed soft X-ray component.

Following OCR, we introduce the mass coordinate

$$M(r,t) = 4\pi \int_{R_*}^{r} \mathrm{d}r'\, r'^2 \rho(r',t). \tag{19}$$

Figure 2 shows density and velocity of the wind model of Fig. 1, now plotted against M. The mass is given here in units of the "photospheric mass",

$$M_{\rm phot} = 4\pi R_*^2/\sigma_e, \tag{20}$$

which is derived by assuming an isothermal, plane-parallel exponential density stratification, with the location of the photosphere at optical depth unity for Thomson scattering.

Figure 2 shows that only a tiny fraction of the wind mass is actually accelerated to high velocities in front of the reverse shocks. Furthermore, almost the whole wind mass is localized within the dense shells. In the velocity run of Fig. 2, the reverse and forward shocks enclosing a shell are clearly separated.

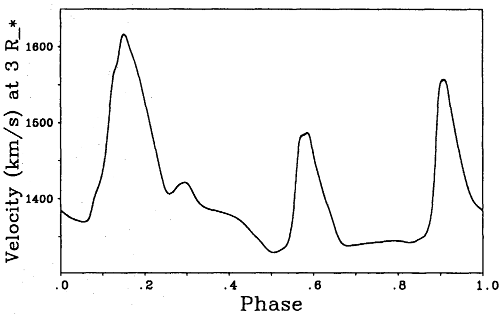

Fig. 3. Time series of the velocity at the fixed location $r = 3\,R_*$ in the wind, plotted against the phase of a wave with period $P = 5\,000$ s. 48.3 wave cycles are shown

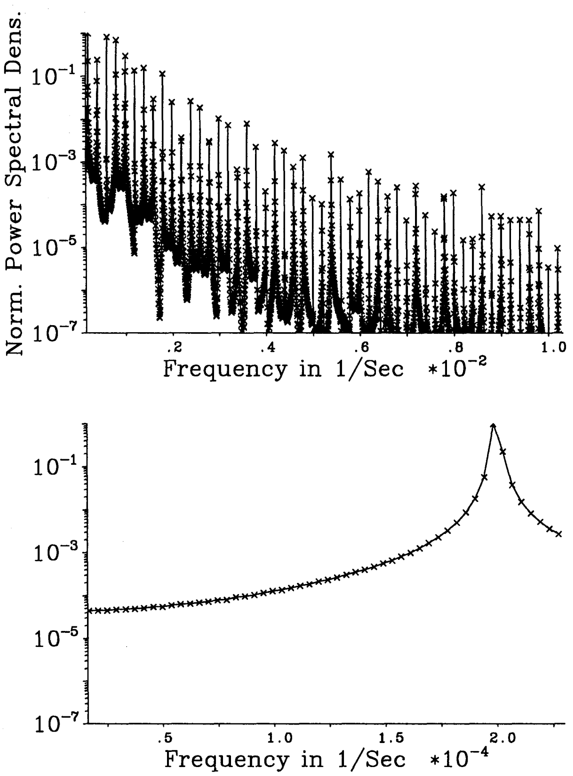

Fig. 4. Power spectrum of the time series of Fig. 3. *Upper panel*: Harmonic domain of the frequency $f = 1/5\,000\,\mathrm{s}^{-1}$ (leftmost peak). The first 50 overtones of this frequency are clearly seen. *Lower panel*: Subharmonic domain of $f = 1/5\,000\,\mathrm{s}^{-1}$ (right peak)

A powerful method to test for the periodic vs. chaotic nature of the wind structure is to analyze time series of hydrodynamical quantities at fixed locations in the wind. Figure 3 shows a time series of the velocity at $r = 3\,R_*$, plotted against the phase of a wave with period $P = 5\,000$ s. The time series starts at $t = 7.20$ days and ends at $t = 10.00$ days, i.e., shows 48.3 wave cycles. It is striking that even within this spatial region, which in the snapshot of Fig. 1 appears to be rather chaotic, the temporal signal is very nearly periodic. As in Fig. 1, one sees 3 shells passing by per 5000 s period. Figure 4 shows the power spectrum of this time series. In the power spectrum, besides the frequency of the photospheric sound wave the first 50 harmonic overtones, $\nu^{(n)} = (n+1)\nu_0$, of this frequency are seen. The reason for the excitation of these overtones is the (nonlinear) wave steepening due to the instability (Landau & Lifschitz 1991, p. 494): though the sound wave is deformed, it keeps its period, so that the Fourier spectrum consists of (all) the harmonic overtones of the wave's frequency. In the subharmonic domain of this frequency no signal is found, see the lower panel of Fig. 4. In particular, no period doubling occurs, which would be a very first hint of a realization of the Feigenbaum route to deterministic chaos (see, e.g., Schuster 1989) in the wind. Furthermore, the acoustic cutoff frequency of $1/6.2\,\mathrm{h}^{-1}$ does not show up. While a corresponding wave *is* present in early times of the simulation, it is damped within a couple of days. This is one reason for the rather long time it takes the wind to settle to a periodic response driven by the *explicit* base perturbation.

4. Collapse of the radiative cooling zone

Trying to repeat the above wind calculations including the energy equation results in the shortcoming that no radiative cooling zones are resolved. The shocks enclosing the shells appear to be isothermal again, whereas simple estimates show that the cooling zones behind strong reverse shocks should be resolved quite well by the numerical grid. In this section, we discuss the two major causes of this behaviour for a simple test flow, and present a method to hinder these defects.

4.1. The thermal instability oscillation

Consider the highly supersonic, plane-parallel flow of an ideal gas against a wall. A shock wave forms which propagates into the gas. Due to radiative cooling of the shock-heated gas the shock comes to a stop and the flow becomes stationary (where $\alpha < 3$ in Eq. (16) is necessary for this). The gas accretes onto the wall in an infinitely thin, infinitely dense layer. The analytical solutions for the stationary cooling zones, for different values of α, are listed in the fundamental paper by Chevalier & Imamura (1982; CI in the following).

A new kind of thermal instability due to radiative cooling was discovered by Langer et al. (1981) in numerical simulations of white dwarf accretion columns (AM Her systems). The linear analysis of this instability was performed by CI. The origin of the instability is the nonlinear dependence of the total cooling length on the immediate post-shock temperature. Detailed descriptions of the mechanism are given in Langer et al. (1982), Gaetz et al. (1988), and Wu et al. (1992). This instability is termed "*global* thermal instability" since it concerns the cooling zone as a whole, in contrast to the "local" thermal instability of Field (1965), which leads to a runaway cooling of single fluid particles. The instability is an oscillatory one (cf. Chandrasekhar 1961), with the cooling zone contracting and expanding periodically, and with the shock front at the very beginning of the cooling zone oscillating around its stationary rest position. The period of this oscillation can be estimated to be (Langer et al. 1982)

$$t_{\mathrm{osc}} \approx 6\, t_{\mathrm{c}}, \tag{21}$$

where t_{c} is again the cooling time. This estimate for the oscillation period is in very good agreement with results from the exact linear stability analysis, which typically gives $t_{\mathrm{osc}} \approx 5\, t_{\mathrm{c}}$, with a slight dependence on α. It is more difficult to derive the maximum value of α for which the oscillatory thermal instability still occurs, since this value depends on the detailed dynamics of the expanding and contracting cooling zone. CI as well as Imamura et al. (1984) find instability for $\alpha \lesssim 0.4$ in the fundamental mode, and for $\alpha \lesssim 0.8$ in the higher modes (see CI for the definition of the different modes). Bertschinger (1986) finds instability for $\alpha \lesssim 1$.

We suggest (cf. Feldmeier 1993, 1994) that the global thermal instability is the major cause for the numerical isothermality of strong shocks in wind simulations including energy transfer. Even if the numerical grid is fine enough to resolve the *stationary* radiative cooling zone, the cooling zone of minimum extent during the contraction phase can fall below the grid resolution. The numerical scheme "forgets" about the existence of the cooling zone then, and the shock becomes numerically isothermal. The reversible oscillation has thereby turned into an irreversible collapse.

To test this hypothesis, we consider the above plane-parallel, radiatively cooling gas flow. The pre-shock density and velocity are fixed to be 1 and -1, respectively. The cooling constant A is chosen so that the *stationary* cooling zone has an extent of $L_{\mathrm{c}} = 1$. The adiabatic exponent is $\gamma = 5/3$, and the Boltzmann constant as well as the atomic weight are both taken to be $k = \mu = 1$. The wall is located at $x = 0$.

Numerical results for the *stationary* cooling zones in case that there is *no* instability ($\alpha \geq 1$) are found to be in good agreement with the analytical solution given by CI. Figure 5 shows a calculation for $\alpha = 1$, and for a Mach number at the shock front of 10^{10} (which is meant to simulate an arbitrarily strong shock; the Mach number of the shock is controlled by the temperature assumed for the pre-shock gas). The position of the shock at $x = 1$ in Fig. 5 is wrong by 1 grid point. This is due to solving the non-conservative thermal energy equation including artificial viscosity.

We define the number "Res" to be the ratio of the length of the stationary cooling zone to the length of a grid interval,

$$\mathrm{Res} = L_{\mathrm{c}}/\Delta x \tag{22}$$

For the *unstable* case $\alpha = -1/2$ now, Fig. 6 shows the run of density, velocity, and temperature at subsequent moments of the oscillation cycle. The left column is for a calculation with Res = 30, the middle column for one with Res = 8; the rightmost column will be discussed below. The snapshots are separated by time intervals $\Delta t = 4$, which is the approximate cooling time, $t_{\mathrm{c}} \approx L_{\mathrm{c}}/v_{\mathrm{post}}$, where $L_{\mathrm{c}} = 1$ and $|v_{\mathrm{post}}| = 1/4$. (Note that the

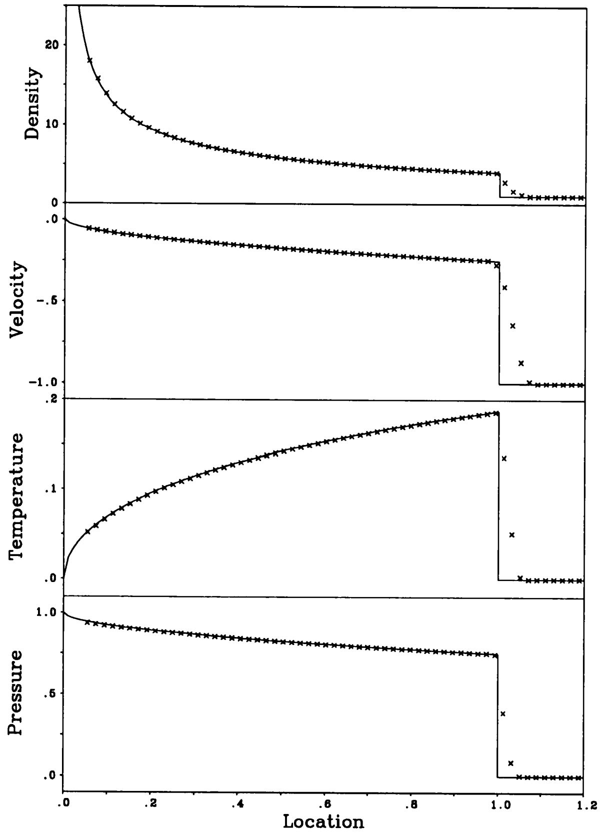

Fig. 5. Normalized (according to Appendix A) stationary radiative cooling zone for the test flow problem described in the text, with a cooling exponent $\alpha = 1$. *Full line*: Analytical solution after Chevalier & Imamura (1982). *Crosses*: Numerical solution

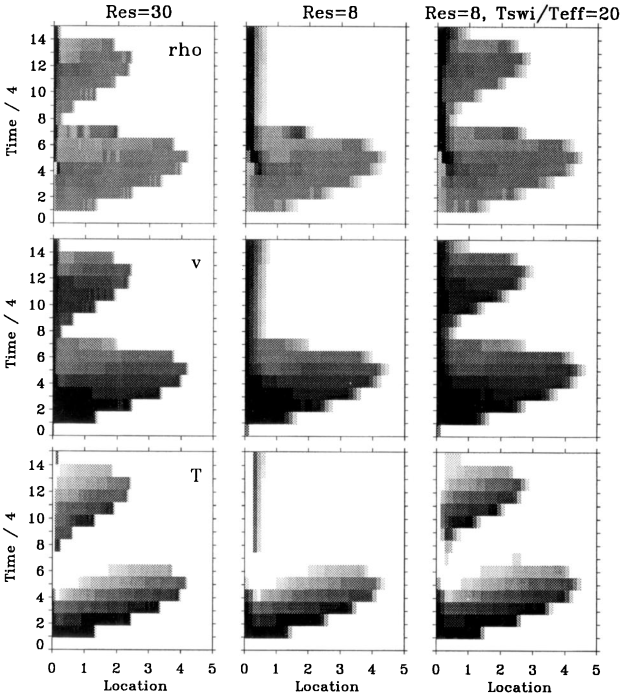

Fig. 6. Global thermal instability oscillations for $\alpha = -1/2$ at grid resolutions Res = 30 (resolved; left panel) and Res = 8 (collapsed; mid panel). The snapshots are separated by the cooling time $t_c = 4$. The right panel is for the same resolution as the mid panel, but now using $T_{\rm swi}/T_{\rm eff} = 20$, resp. $T_{\rm post}/T_{\rm swi} = 5$. This hinders the collapse of the cooling zone

time axis in Fig. 6 is in units of $t_c = 4$.) The last snapshot is for $t = 60$, corresponding to 2 oscillation cycles.

Immediately after $t = 0$, a shock front is created which propagates away from the wall. The density on the first two or three grid points is much too low, whereas the temperature is too high. This is Noh's (1987) artificial *wall heating*, caused by the use of artificial viscosity. During the first 3 cooling times, the run of velocity, density, and temperature within the cooling zone approaches the analytical solutions for a *stationary* cooling zone. Yet, after about 4 to 5 cooling times both the velocity and density become nonmonotonic, and *secondary shocks* (cf. Falle 1975, 1981; Gaetz et al. 1988) form close to the wall. The cooling zones of these secondary shocks are not resolved in the present calculation, so they appear to be isothermal shocks; however, their resolution could easily be achieved by using a finer grid, (see Feldmeier 1993). After 5 cooling times, the primary shock at the very beginning of the cooling zone starts to propagate in direction of the wall. The maximum possible shock speed is the speed of the inflowing material, since otherwise the pre- and post-shock domain would interchange. The shock in fact almost reaches this maximum speed, at which moment hardly any temperature jump is seen ($t = 7\,t_c$). At $t = 8\,t_c$, the cooling zone has its minimum extent. Since the shock speed is zero then, the temperature jump is the same as for a stationary shock, $T_{\rm post} = 3/16$. On a sufficiently fine grid, the shock starts propagating away from the wall again (left column of Fig. 6), whereas on a coarse grid the shock collapses at the wall (mid column). In the latter case, the temperature jump of 3/16 is still found, but over the next 2 (or 3) grid intervals the material cools again to $T = 0$. Since already the (artificial) viscous shock layer is ≈ 3 grid intervals broad, this cooling zone is *not* resolved, hence the shock must be considered as a numerical isothermal shock.

4.2. Shock front cooling and advective diffusion

There is another numerical defect which might be responsible for the collapse of the cooling zones. The material of intermediate temperatures within the *artificially broadened* viscous shock layer cools more efficiently than the hot post-shock material. This could lead to an "eating" of the shock front into the cooling zone, and therefore a collapse of the latter. However, in appendix 6 it is shown that for a cooling exponent $\alpha = -1/2$, strong cooling within the viscous layer only takes place if the *post-shock* temperature implies that the cooling zone is narrower than the viscous layer. In this case, the cooling zone cannot be resolved on the grid anyway, since even the viscous layer is unresolved. Consequently, no enhanced cooling problem should exist in shock fronts followed by a cooling layer broader than a few grid distances.

Yet another mechanism which *is* possibly related to the cooling zones' collapse is *advective diffusion* (Owocki, priv. comm.). This defect would explain the observed influence of *advection* on the collapse (Feldmeier 1993, p. 185). We suggest that advective diffusion occurs at the *cold end* of the cooling zone, instead of occuring at the shock front as proposed by Owocki. Our reasoning has two parts: (i) Due to Field's (1965) cooling runaway, the temperature (and density) gradient is *infinite* at the cold edge. Therefore, a positive feedback between the diffusive errors of the numerical advection scheme and enhanced radiative cooling occurs. Interpolation errors of the advection scheme smear out the edge; since for small α the cooling rate is larger at smaller temperatures, the smeared out edge becomes steep again, thereby "eating" a certain distance into the cooling zone. At the sharp edge, then, new diffusive errors build up, etc. (ii) The speed is *continuous* at the cold edge, i.e., the same material always lies there (with new material being added constantly), and so the errors are *additive*. This is in contrast to shock fronts, where new particles always pass through, and errors *converge* to a certain value.

Loosely speaking, the cooling zone is destroyed from both ends: (i) from the oscillating shock side, due to the collapse during the contractional phase of the global thermal instability; and (ii) from the cold edge, due to the interplay between numerical diffusion and radiative cooling.

4.3. Modification of the cooling function

To hinder the collapse of the cooling zone caused by the oscillatory thermal instability, we propose the following procedure. The radiative cooling function is modified in the way shown in Fig. 7, namely: (i) Below a certain temperature $T_{\rm swi}$ the cooling function is assumed to have a *stable* slope $\alpha = +2$. (ii) At $T_{\rm swi}$ itself, the cooling function must be continuous, and this defines the cooling constant $\tilde{A}$ below $T_{\rm swi}$,

$$\tilde{A} = A T_{\rm swi}^{-5/2}. \tag{23}$$

The most critical time interval during the contraction of the cooling zone is defined by the following two instants: It *starts* at about the moment when the shock has almost disappeared because of propagation in the direction of the cold edge with the same speed as the incoming material; and it *ends* with the ultimate collapse of the cooling zone due to the shock approaching the cold edge. During the first moments of this time interval the material within the *whole* cooling layer radiates energy according to the *stable* cooling function with $\alpha = 2$ slope; at later times, it is still the material sufficiently close to the cold edge radiating according to an $\alpha = 2$ power law. Therefore, the shock's propagation in the direction of the cold edge is decelerated by the build up of excess pressure, so that the shock cannot approach the edge too closely. In addition to the stability of the $\alpha = 2$ slope, a further deceleration of the shock is caused by the lower cooling rate at $T < T_{\rm swi}$ of the modified as compared to the original cooling function – necessitating broader cooling zones.

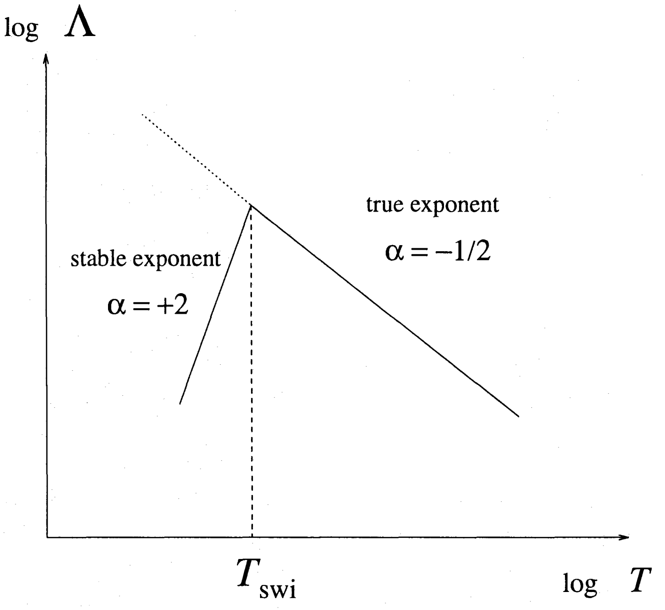

Fig. 7. Modification of the radiative cooling function at low temperatures, to hinder the collapse of the cooling zone

The right column of Fig. 6 shows a calculation with $T_{\rm swi}/T_{\rm eff} = 20$. The collapse is hindered, and the cooling length as well as the structure of the cooling zone agree well with those in the left column of Fig. 6, where the original cooling function with $\alpha = -1/2$ slope has been used on a finer grid.

Since *hot* gas radiates energy according to the original cooling function, the influence of the modified cooling function on the observed X-ray emission from the gas behind strong shocks in time-dependent stellar wind simulations should be small. More critical is the influence of the modification on the total cooling length. Since the material cools inefficiently at low temperatures, the cooling zones might be broadened artificially. We will now show that the influence of the low-temperature $\alpha = 2$ slope on the total cooling length is small.

The time needed for hot, shocked material to cool down again to wind temperature $T_{\rm eff}$ is,

$$t_{\rm c} = \int_{T_{\rm post}}^{T_{\rm eff}} {\rm d}t_{\rm c}. \tag{24}$$

The thermal energy equation for a fluid particle is (with ${\rm d}/{\rm d}t$ the Lagrangian derivative, and $\epsilon = e/\rho$ the specific thermal energy),

$$\rho \frac{{\rm d}\epsilon}{{\rm d}t} = -p \,{\rm div}\, {\bf v} - A\rho^2 T^\alpha. \tag{25}$$

It is well known (e.g., Langer et al. 1981; CI) that the divergence term in (25) leads to near *pressure constancy* within the cooling zone. We therefore drop this term and instead assume the pressure to be constant,

$$\rho \frac{{\rm d}\epsilon}{{\rm d}t} = -A\rho^2 T^\alpha, \qquad \text{with} \qquad p = {\rm const} = p_{\rm post}. \tag{26}$$

This leads to

$$\mathrm{d}t_\mathrm{c} = -\frac{k^2}{\mu^2(\gamma-1)}\, p_\mathrm{post}^{-1}\, \frac{\mathrm{d}T\, T^{1-\alpha}}{A}, \tag{27}$$

where the kinetic equation, $\epsilon = kT/\mu(\gamma-1)$, and the ideal gas equation have been used. The cooling length is

$$L_\mathrm{c} = \int_{T_\mathrm{post}}^{T_\mathrm{eff}} \mathrm{d}t_\mathrm{c}\ \mid v_\mathrm{rel} \mid, \tag{28}$$

where the relative velocity between shock front and material behind the shock, v_rel, can be approximated by v_post, so that

$$L_\mathrm{c} = v_\mathrm{post}\, t_\mathrm{c}. \tag{29}$$

Let R be the ratio of the total cooling length using the modified cooling function to the cooling length using the original cooling function, i.e., without the modification below T_swi. The velocity v_post then cancels in R. Using (23) for the constant $\tilde{A}$, one has

$$R = \frac{\int_{T_\mathrm{post}}^{T_\mathrm{swi}} \mathrm{d}T\, T^{3/2} + \int_{T_\mathrm{swi}}^{T_\mathrm{eff}} \mathrm{d}T\, T^{-1}\, T_\mathrm{swi}^{5/2}}{\int_{T_\mathrm{post}}^{T_\mathrm{eff}} \mathrm{d}T\, T^{3/2}}. \tag{30}$$

Introducing dimensionless quantities,

$$t = T/T_\mathrm{eff}, \qquad t_\mathrm{s} = T_\mathrm{swi}/T_\mathrm{eff}, \qquad t_\mathrm{p} = T_\mathrm{post}/T_\mathrm{eff}, \tag{31}$$

this becomes finally

$$R = \frac{{t_\mathrm{p}}^{5/2} - {t_\mathrm{s}}^{5/2} + \frac{5}{2}\, {t_\mathrm{s}}^{5/2} \ln t_\mathrm{s}}{{t_\mathrm{p}}^{5/2} - 1}. \tag{32}$$

$$\approx 1 + \left(\frac{t_\mathrm{s}}{t_\mathrm{p}}\right)^{5/2} \left[\frac{5}{2}\ln t_\mathrm{s} - 1\right], \tag{33}$$

where in the last equation the strong shock approximation, $t_\mathrm{p} \gg 1$, has been used. Table 2 lists R as function of t_p and t_s.
The physical reason for the weak dependence of the total cooling length on T_swi found in Table 2 is that the extent of the cooling zone is fixed mainly by the material immediately behind the shock, which cools according to the original $\alpha = -1/2$ slope: since this material is thin (cooling rate $\sim \rho^2$) and hot (cooling rate $\sim T^{-1/2}$) it cools very inefficiently. Altogether, because of the dominance of the hot post-shock material (i) on the X-ray emission from stellar winds, and (ii) on the total cooling length, the modification of the cooling function below T_swi has actually only little influence on the model results.

Finally, we note that the $\alpha = 2$ slope below T_swi also hinders the collapse of the cooling zone due to the positive feedback between diffusive errors and enhanced radiative cooling at the *cold edge* of the cooling zone: As was shown by Field (1965), runaway cooling only occurs for $\alpha < 2$ if the gas cools isobarically. By this, using $\alpha = 2$, cooler material no longer cools more efficiently. Therefore, the cold edge remains smeared out, instead of being steepened again (which would cause new advective errors, and the edge to "eat" into the cooling zone).

Table 2. Dependence of the total cooling length on the temperature T_swi. R is the ratio of the cooling length using a modified cooling function below T_swi to the true cooling length.

$T_\mathrm{post}/T_\mathrm{eff}$	$T_\mathrm{swi}/T_\mathrm{eff}$	$R = \frac{L_{c,\mathrm{swi}}}{L_{c,\mathrm{true}}}$
300	10	1
	20	1
	30	1
200	10	1
	20	1
	30	1.1
100	10	1
	20	1.1
	30	1.4
50	10	1.1
	20	1.7
	30	3.1
40	10	1.1
	20	2.1
	30	4.7
30	10	1.3
	20	3.4
	30	8.5

5. Wind models including energy transfer

In this section, we use the same stellar, wind, and numerical parameters as in Sect. 3, and discuss three different wind models:

1. A model using the radiative cooling function (16) with an overall $\alpha = -1/2$ slope.
2. A model where this slope is changed to be $\alpha = +2$ below $T_\mathrm{swi}/T_\mathrm{eff} = 10$.
3. The same model as in 2, but with an amplitude of the photospheric sound wave of 25% instead of 1%.

5.1. Estimate of cooling lengths

We use Eq. (A9) from appendix A to estimate whether the spatial grid in wind simulations is fine enough to resolve typical stationary cooling zones. With the parameters from Table 1 we find

$$\frac{L_\mathrm{c}}{R_*} = 1.47\, 10^{-7}\, \frac{r^2}{R_*^2} \left(1 - \frac{R_*}{r}\right)^{\beta} \frac{(T_\mathrm{post}/T_\mathrm{eff})^2}{\rho_\mathrm{pre}/\rho_\mathrm{stat}}. \tag{34}$$

We use $\beta = 0.8$ (Pauldrach et al. 1986) for the underlying mean wind velocity law. Actually, the stationary velocity run in the snapshots of the wind structure in Figs. 1, 2, 8, etc. is, beyond the sonic point, the one of a $\beta = 0.8$ law. Table 3 lists the total cooling length (34) as function of the post-shock temperature and the depletion of the wind material relative to a stationary wind model, at the location $r = 4\, R_*$. The number of grid points per cooling zone is given in brackets. According to this table, *all* stationary cooling zones behind *strong* shocks should be resolved on the grid.

Table 3. Total cooling length (in units of R_*) as function of the post-shock temperature and the depletion of the wind material relative to a stationary wind model, at the location $r = 4\,R_*$. The number of grid points per cooling zone is given in brackets.

	$\frac{T_{\rm post}}{T_{\rm eff}}$=25	50	100	200
$\frac{\rho_{\rm pre}}{\rho_{\rm stat}}$=1	0.0012 (0.4)	0.0047 (1.5)	0.019 (6)	0.075 (24)
1/10	0.012 (4)	0.047 (15)	0.19 (62)	0.75 (240)
1/100	0.12 (39)	0.47 (150)	1.9 (620)	7.5 (2400)

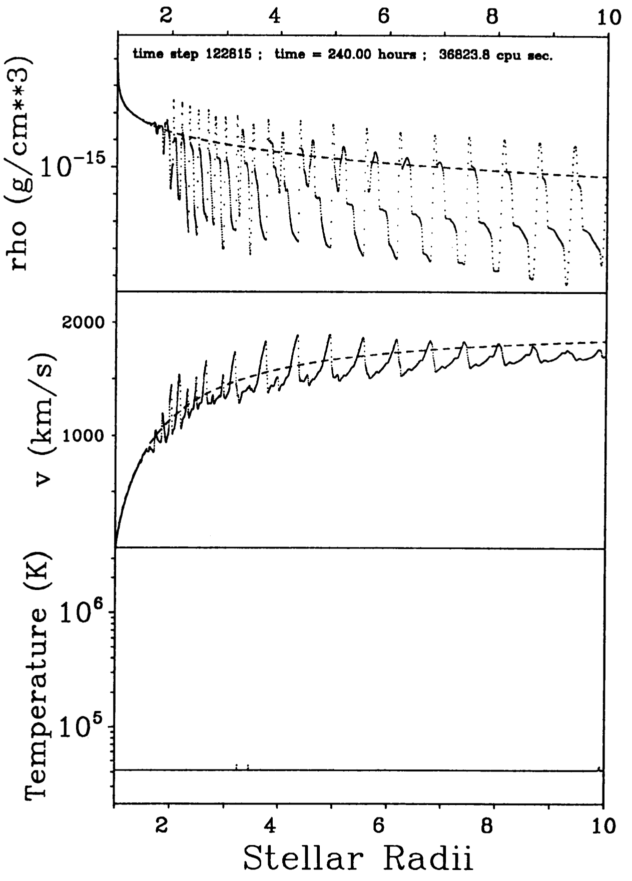

Fig. 8. Snapshot of the wind structure with energy equation included, but without modifying the cooling function at low temperatures. All cooling zones behind shocks are collapsed

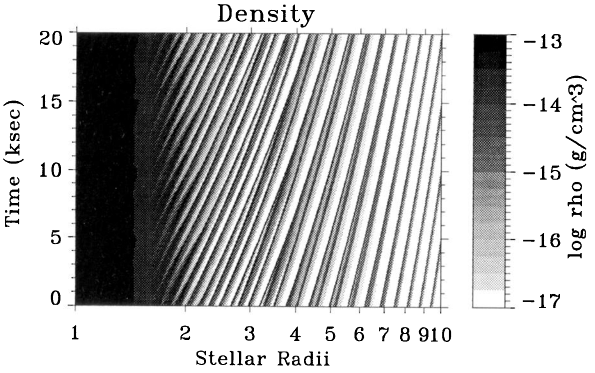

Fig. 9. Evolution of the wind structure from Fig. 8 (using an unmodified cooling function with slope $\alpha = -1/2$) during the next 20 000 s, i.e., 4 cycles of the photospheric sound wave

5.2. The wind models

Figure 8 shows a snapshot of the wind 10 days after model start. The cooling function used is the one of Eqs. (16) and (17). Figure 9 shows the subsequent evolution of the density in the course of 20 000 s, i.e., four cycles of the photospheric sound wave.

No cooling layers behind shock fronts are resolved in Fig. 8. (Since already in this snapshot no hot gas is present, we do not show the run of temperature during the wind evolution in Fig. 9.) This is in accord with our expectation of the cooling zones' collapse. In Figs. 10 and 11 then, where a modified cooling function is used below $T_{\rm swi}/T_{\rm eff} = 10$, i.e., 420,000 K, this collapse is hindered and the cooling zones are well resolved. Figure 1 and Fig. 8 show almost identical wind structures; this is clear from the fact that both models are *isothermal* calculations in the end. (Small differences occur in extremely rarefied intershell regions, which contain hardly any material.)

Up to about 4.5 to 5 R_*, the isothermal wind model(s) and the model with resolved cooling zones are also very similar. The reason is that the cooling zones are short compared with dynamical length scales, which supports the assumption of dynamical isothermality for dense supergiant winds in this spatial domain.

However, the cooling layers in this model are (much) shorter than what would be expected from Table 3. This is (mainly) due to the fact that the *dynamical* time required to deplete the intershell regions by adding the material located there to the narrow shells (which is accomplished by the radiative shocks) is shorter than the *cooling* time. The analytical solution for a *stationary* cooling zone from Appendix A therefore does not apply. Due to this intershell depletion, the pre-shock density becomes smaller with time, so that a broader cooling zone has to be established. The time necessary for this is of the order of the period of the thermal instability oscillation – which in turn is a few cooling times –, i.e., (much) larger than the dynamical time. Therefore, the cooling zones lag behind the actual dynamical situation, and one should observe them to be *shorter* than stationary cooling zones – as is actually the case.

Beyond about 5 R_*, the model with energy transfer differs drastically from the isothermal model. Consider the four rarefied intershell regions marked (a) to (d) in Fig. 10. It is within this sequence that *all* shocks in the wind are destroyed, leaving behind only *previously* heated material: At (a), a pronounced radiative shock is present; the material is heated in a front, and afterwards cools by radiative energy losses. Since the cooling zone is approximately isobaric, the density rises with falling temperature, which leads to the final compression of the material into a narrow, dense shell. From (a) to (b), the pre-shock density drops by about a factor of 6 due to the intershell depletion. This causes a broadening of the cooling layer, whereby

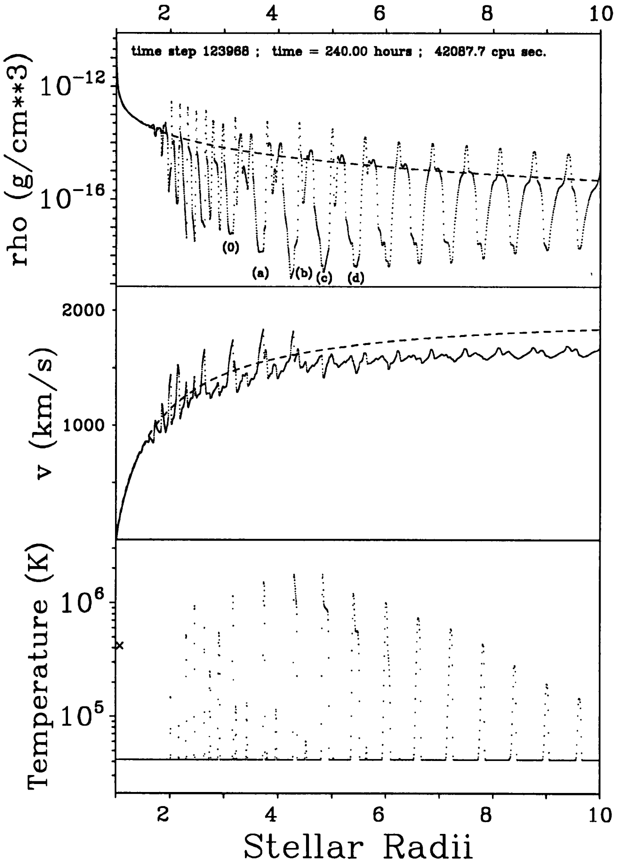

Fig. 10. Snapshot of the wind structure, where the cooling function is modified below $T_{\rm swi}/T_{\rm eff} = 10$ to have a slope $\alpha = 2$. The cross near the temperature axis indicates $T_{\rm swi}$

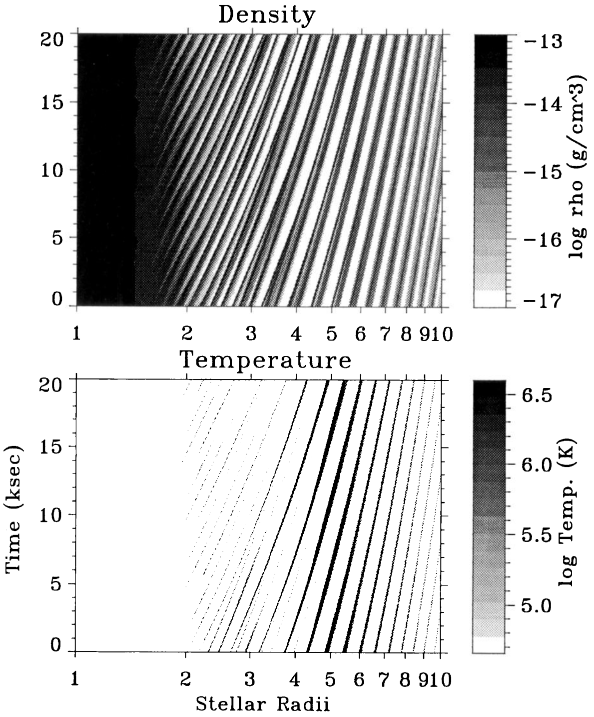

Fig. 11. Evolution during the next 20 000 seconds (after t = 10 days) of the model with $T_{\rm swi}/T_{\rm eff} = 10$ and amplitude $A = 1\%$

the shock front is driven in the direction of smaller radii, into the unshocked material. The pre-shock velocity and post-shock temperature therefore get slightly larger from (a) to (b). However, for later times the inward moving front passes regions of always slower material, until finally the front speed equals the speed of the inflowing material and the shock vanishes at (d): the temperature "jump" at (d) is about 10 grid intervals broad, instead of 3 intervals at a shock front; furthermore, no velocity jump is found at (d). The propagation of the front to smaller radii is directly seen in the sequence from (b) to (d), where the shock passes from the right side of the density minimum of the intershell region to its left side. The hot material at (d) (and at all larger radii) is the *remnant* of *previously* shock-heated material. This interpretation is supported by the fact that the density and temperature at (d) and at all larger radii are anti-correlated, as is the case in the isobaric radiative cooling zone behind a shock. The hot material then cools steadily by radiative energy losses and spherical expansion work during its further advection to larger radii. (We finally note that due to intershell depletion, the cooling zone at (a) is already broader than the corresponding one at (0); but not yet broad enough to destroy the shock front.)

The observational consequences of this shock destruction for the X-ray emission properties can only be tested by quantitative modeling of the X-ray spectra from structured wind models – this work is in progress now. We recall that already in the isothermal wind model shock *decay* (as opposed to shock destruction) sets in at about 5 R_*. In all models up to now therefore the bulk of X-ray emitting material is at small radii. This is in contrast to what is derived from ROSAT X-ray observations: Hillier et al. (1993) find that in the wind of ζ Pup, material with temperatures $T = 3\,10^6$ K has to be present up to radii of 20 to 50 R_*. One reason for the failure of our models to produce hot material beyond a few R_* is the small amplitude of only 1% of the photospheric sound wave. This will be seen below from a model with an amplitude of 25%. Besides that, the period of the sound wave also has an influence on the maximum temperatures that occur (Owocki 1992; Feldmeier 1993): for large periods, the shell distances are larger, and the material in between the shells can be accelerated to higher velocities before it finally encounters a reverse shock. So, at present we do not expect a real conflict between X-ray observations and the time-dependent wind models.

The mean velocity of the model with resolved cooling zones is somewhat smaller than the stationary wind velocity. This is mainly due to the fact that radiative driving is shut off for hot material. Furthermore, shadowing by material close to the star might be slightly more efficient in this model.

Up to about 4 R_* the wind structure in the model with resolved cooling zones seems to be as chaotic as in both isothermal models. However, from Figs. 9 and 11 it is evident that the cause of this are *shell-shell collisions*. The shells are created at $\approx 1.5\,R_*$ in *triples*, where the members of these triples collide

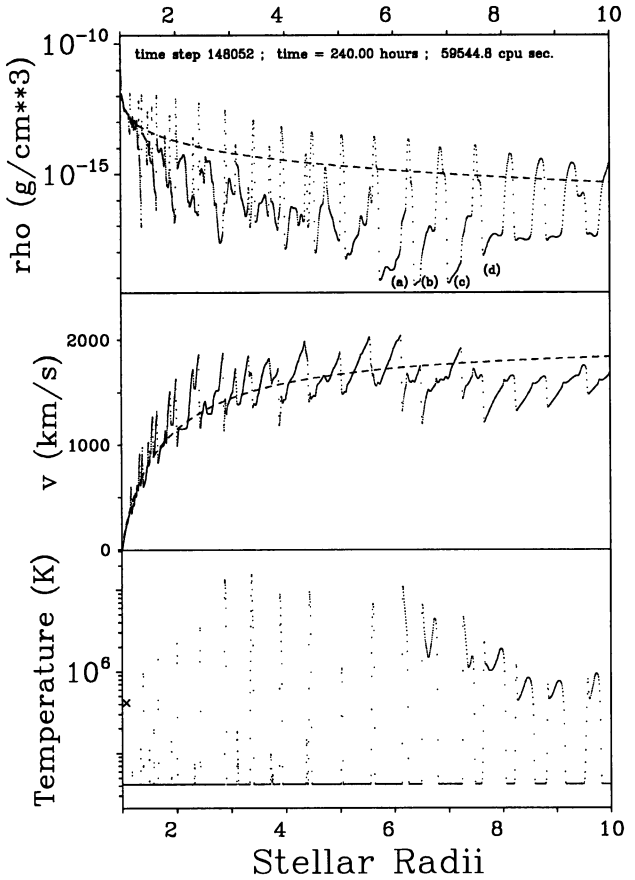

Fig. 12. Wind snapshot using a modified cooling function below $T_{\rm swi}/T_{\rm eff}$ = 10. The amplitude of the photospheric sound wave is 25% now instead of 1% in the foregoing model

with each other, leaving only one shell per cycle of the photospheric sound wave beyond $\approx 6\,R_*$. There are no collisions between shells steming from subsequent cycles of the sound wave. We note that the shells would not collide if they simply "ride" the wind (Waldron et al. 1992, 1994). For shell collisions to occur, two requirements have to be met: (i) The shells influence each other ("non-local coupling"). This is actually the case in the time-dependent models since shells lying close to the star shadow, and therefore decelerate, shells at larger radii. (ii) The shells do *not* follow each other at constant time intervals. This is realized in the wind because of the triple-wise creation of shells; which, in turn, is connected to the excitation of harmonics of the photospheric sound wave that triggers structure formation. – It is easily seen that if either of these prerequisites is not fulfilled, shell collisions cannot occur; instead, all shells would follow (almost) the same path $r_{\rm shell}(t)$.

To test the influence of the amplitude A of the photospheric sound wave on the shock strength, Figs. 12 and 13 show a snapshot at t = 10 days and the subsequent evolution over 20 000 s of a model with A = 25%. Maximum temperatures are now a factor of 10 higher than for A = 1%, and reach 2 10^7 K between 3 and 6 R_*.

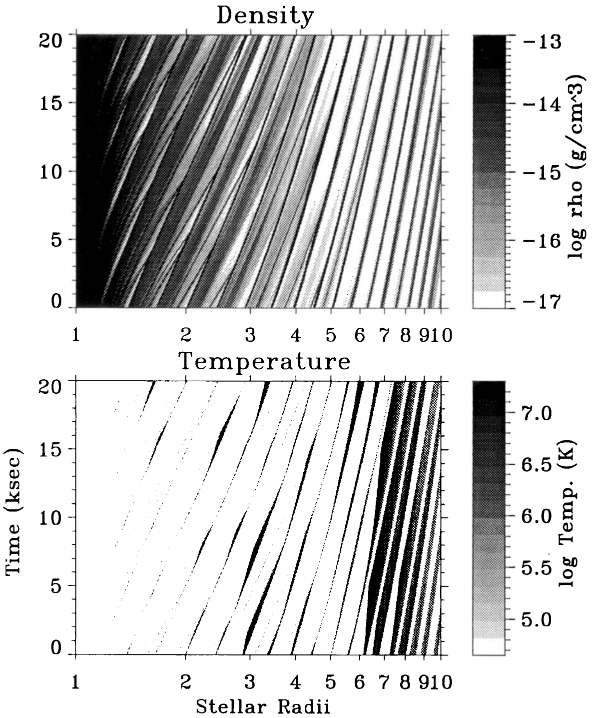

Fig. 13. Evolution during the next 20 000 seconds (after t = 10 days) of the model with amplitude A = 25%

Up to about 6 R_* dynamical isothermality should be a good approximation for this model. However, shock destruction due to the broadening of cooling zones occurs around $\approx 7\,R_*$, see the sequence from (a) to (d) in Fig. 12. At (a) and (b) radiative shocks are found, where the pre-shock density falls by a factor of 16 from (a) to (b). The corresponding broadening of the cooling zone is obvious from the temperature run of Figs. 12 and 13. The shock is driven to smaller radii, until it finally disappears at (d). The velocity jumps separating cold, dense gas from hot, thin gas (formerly heated in shocks) are due to the fact that the hot gas is no longer radiatively driven, wherefore the cold, fast gas rams into it supersonically. (Since post-shock temperatures are much lower in the previous A = 1% model, the corresponding drop in the radiative acceleration is not so significant there.) These *forward* shocks heat the already hot material to even higher temperatures; thereafter, the gas is cooled and compressed by radiative energy losses. The forward shock transition + radiative cooling zone is best seen in the temperature spike at the left verge of the hot, thin regions at $r > 7.5\,R_*$. (These points were brought to our attention by S. Owocki.) – Note that the hot gas left over at 10 R_* still has a temperature of $\approx 10^6$ K. This is not too different from what is needed to model the ROSAT X-ray observations of ζ Pup (Hillier et al. 1993).

The structure formation in this model sets in closer to the star, at about 1.2 R_* instead of 1.5 R_* in the previous model. The shells are created in *quadruples* close to the star, where the members of these quadruples collide up to 3 R_*. There is some dynamical coupling between shells corresponding to *subsequent cycles* of the sound wave now: Relatively dense material in front of the forward shock side of one shell can be accelerated, after which it moves through the strongly rarefied intershell medium and finally collides with the reverse shock side of the next-outer shell. The last shell collisions occur between 6.5 to 7 R_*.

There is a definite temporal *non*-periodicity in Fig. 13. Figures 14 and 15 show the time series of wind velocity at 3 R_* (plotted against the phase of a wave with period $P = 5\,000$ s) and its power spectrum. The time series starts at 7.82 days and ends at 10.00 days, i.e., shows 37.7 wave cycles. The contrast to Figs. 3 and 4 for the time series and spectrum of the model with a base perturbation amplitude of $A = 1\%$ is striking. A major effect in Fig. 14 seems to be a *drift* of the wave. Since in the power spectrum of the $A = 1\%$ model signals (i.e., the harmonics of the sound wave) and noise (if there is any) are separated by 4 orders of magnitude, we must conclude that the "noise" in Fig. 15 has physical meaning and is not caused numerically. The source of this non-periodicity is not exactly clear at the moment, but seems to be connected with the coupling of shells from subsequent wave cycles. It is found (Owocki & Feldmeier, in prep.; Owocki 1995) that *without* any explicit perturbation at the base, *small-scale* structure develops in the wind from about 2 R_* on. This structure also shows a *continuous* spread of wave frequencies. In the cases of no perturbation, a broad-band perturbation, or a large-amplitude periodic perturbation, frequencies over a broad interval may principally grow on equal footing, since: (i) The instability growth rate is constant for all wavelengths shorter than a certain fraction ($\approx \frac{1}{3} \dots \frac{1}{2}$) of the Sobolev length (Owocki & Rybicki 1984, 1985). (ii) For zero perturbation amplitude it seems natural to assume that *numerical noise* (showing a continuous spread of frequencies) is created and amplified. On the other hand, for large base perturbation amplitudes, we speculate that some kind of *overmodulated* amplification occurs, again creating noise.

Whether a periodic or a stochastic ("turbulent") wind structure is realized depends fundamentally on the value of the non-dimensional "Reynolds" number connected with the wind instability. While the radiation field is the central quantity entering this number, to our knowledge no precise definition of the latter has been given up to now. However, the strong periodicity of the wind structure induced by *small* (here: $A = 1\%$) perturbations – as they are considered in *linear* stability analysis – gives a hint that the radiation Reynolds number of our models is still below the threshold(s) required for multi-mode excitation or stochastic behavior.

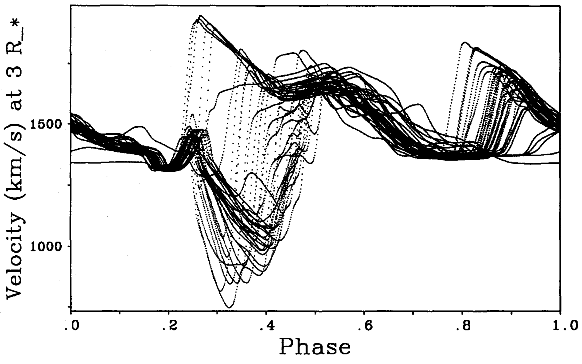

Fig. 14. Time series of the velocity at $r = 3\,R_*$ of the model with base perturbation amplitude $A = 25\%$, plotted against the phase of a wave with period $P = 5\,000$ s. 37.7 wave cycles are shown

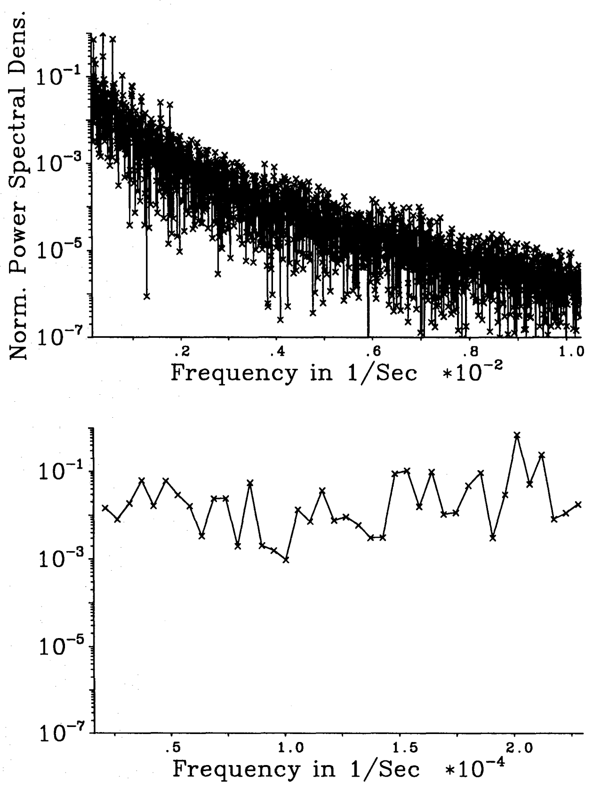

Fig. 15. Power spectrum of the time series of Fig. 14. *Upper panel*: Harmonic domain of the frequency $f = 1/5\,000\,\mathrm{s}^{-1}$. *Lower panel*: Subharmonic domain

The question remains whether the contraction and expansion of the cooling zones due to the oscillatory thermal instability can be seen directly in the wind models. The period of this oscillation is $t_{\rm osc} \approx 20\,L_{\rm c}/v_{\rm jump}$, where $L_{\rm c}$ is the cooling length, and $v_{\rm jump}$ is the velocity jump at the shock front. For the model with $A = 1\%$, the oscillation periods should be about 10 to 30 hours, and for the $A = 25\%$ model $\approx$ 3 to 10 h. Each shock in Fig. 11 ($A = 1\%$) could be followed over $\approx$ 7 h, which is *less* than $t_{\rm osc}$. Furthermore, the dynamical time scale for shell-shell collisions, $t_{\rm coll} \approx 5 \dots 6$ h, is shorter than $t_{\rm osc}$. Hence, the thermal oscillation is also unobservable since changes in the shock properties due to shell-shell collisions take place in shorter times than $t_{\rm osc}$. In Fig. 13 for the $A = 25\%$ model, each shock could be followed over almost 15 hours before it is finally destroyed at $\gtrsim 7\,R_*$. During that time, 1 to 2 thermal oscillations should occur. However, $t_{\rm coll}$ is even shorter in this model (shell quadruples instead of triples; interaction between shells from different cycles of the sound wave), and ranges from $\approx$ 1 h close to the star to 4 h at larger distances. The thermal oscillation is therefore interrupted again. – To be more precise, $t_{\rm osc}$ and $t_{\rm coll}$ of the very narrow cooling zones, $L_{\rm c} \approx 0.02\,R_*$, at $\approx 4\,R_*$ are about equal (few hours). But these cooling zones are only resolved by ≈ 10 grid points, and numerical insufficiency becomes probable: as is found in simulations of the test flow problem from the previous section, modifying the cooling function below $T_{\rm swi}$ hinders the collapse of the cooling zone during the *first* oscillation cycle. Thereafter, a more or less *stationary* cooling zone often remains. Furthermore, we observed a strong damping of the thermal oscillation due to the *advection* of the shock across the numerical grid.

In summary, we believe that a mixture of physical and numerical effects causes the thermal oscillation to be unobservable in our calculations.

6. Summary

In this paper we have discussed time-dependent radiation driven winds of hot, luminous stars, where flow structures are due to the nonlinear, unstable growth of initially small, periodic base perturbations. We have found the following results for the fully developed wind structure:

1. Our models are in good general agreement with the ones by OCR and Owocki (1992, 1994): The wind consists of a sequence of dense, narrow shells which are enclosed by a reverse shock at the starward-facing side and by a forward shock at the outer side. The reverse shocks can have Mach numbers from 30 to 100, implying density contrasts of up to 10^3 to 10^4. The latter value is close to the principal upper limit for a wind with Mach number ≈ 100. The jump velocities of about 500 km/s at the reverse shocks agree well with the shock temperatures of some million degrees K as deduced from X-ray data (Cassinelli & Swank 1983; Hillier et al. 1993).

2. Shell-shell collisions are frequent up to $6 \ldots 7\,R_*$. For these collisions to occur, it is necessary: (i) that the shells influence each other, e.g., by shadowing of the radiation field; and (ii) that the shells do not follow each other at constant time intervals.

3. The wind structure induced by a periodic base perturbation of *small amplitude* is also periodic. The power spectra of long time series of hydrodynamical quantities at fixed locations in the wind indicate the existence of only *discrete* harmonics (up to 50 and more) in this case. In contrast, for a *large amplitude* base perturbation, and also for the case of *no* explicit perturbation at all, the power spectra of the wind structure show a continuous spread of excited frequencies. The hierarchy of shock-shock mergers (or, stated differently: shell-shell collisions) occuring then resembles the picture of *compressible turbulence* as discussed by Burgers (1950) and Tatsumi & Tokunaga (1974). Empirical evidence for turbulence in dense Wolf-Rayet star winds in the form of a mass hierarchy of clumps is described by Moffat (1994a,b).

4. Inclusion of *energy transfer* in the hydrodynamical simulations results in the numerical shortcoming that no radiative cooling zones are resolved. The main cause of this collapse is the oscillatory thermal instability of Langer et al. (1981, 1982). During the *contraction* phase of this oscillation, the extent of the cooling zone may fall below the grid resolution. Consequently, the numerics "forgets" about the existence of the cooling zone, and the shock becomes a numerical isothermal shock. The reversible oscillation has turned into an irreversible collapse. – Furthermore, at the cold, dense end of the cooling zone, a positive feedback between advective diffusion errors and radiative cooling might occur. This leads to an "eating" of the cold edge into the cooling layer, accelerating the destruction of the latter.

5. Both the collapse caused by the oscillatory thermal instability and by the advective diffusion can be hindered by modifying the cooling function at low temperatures. Because the extent of the cooling zone is predominantly fixed by the hot and thin post-shock material – which is also responsible for the X-ray emission –, this modification at low temperatures has minor influence on the derived model results.

6. Up to about 5 to $7\,R_*$ (where the exact value depends on the base perturbation), the assumption of dynamical isothermality is found to be valid in our models of an O supergiant wind: radiative cooling zones behind strong shocks are short compared with dynamical length scales, and therefore have little influence on the wind dynamics. However, beyond these radii dynamical isothermality breaks down completely: all reverse shocks are quickly destroyed due to a broadening of the cooling zone, leaving behind previously heated hot, thin material. This material cools on its further advection through the wind. The question arises whether there is enough hot gas left at large radii to account for the observed soft X-ray component.

7. Quite independent of the amplitude of the base perturbation, the final shell-shell collisions occur between 6 to $7\,R_*$. Together with the results from the item (6) above, the wind can therefore be divided roughly into two distinct regions: an inner, active one with frequent radiative shocks, where shell-shell collisions occur; and an outer, quiescent region with "old" hot material left over from former shock heating, and where the shells follow each other without further collisions. Since the wind dynamics is rather predictable at large radii, the results computed explicitly here up to $10\,R_*$ could be extrapolated to larger distances from the star (e.g., to permit the calculation of X-ray spectra from a very large volume of the wind).

Our two main directions for *future work* on the radiation hydrodynamics of hot star winds are the following:

(I) While the modification of the cooling function below $T_{\rm swi}$ can hinder the collapse of cooling zones, we also plan to incorporate a *local mesh refinement* method (Berger & Oliger 1984; Berger & Colella 1989) in our code as an independent way to avoid the collapse. Applying the latter method, two other resolution problems occuring in time-dependent wind calculations could possibly be solved too: (i) The dense shells, in which most of the wind mass is localized, are poorly resolved in present calculations. (ii) The arbitrary exponential truncation of the line distribution function at $\kappa_{\rm max}$ is needed to artificially suppress unstable growth on very short length scales. The correct treatment of the latter small-scale structure might influence the large-scale dynamics of the wind, as is well known from turbulent flows.

(II) At present, using the SSF method, the source function is not calculated consistently from the actual wind dynamics. In particular, the perturbation of the diffuse radiation field is not accounted for. As found by Owocki & Rybicki (1985), this perturbation has a large influence on the phase relationship between perturbations in velocity, density, and the radiative force, i.e., on the propagation and growth characteristics of waves in the wind (a fact recently emphasised by Puls 1993). For wavelengths on the order of the Sobolev length, *correlated* density and velocity perturbations may thereby grow at an enhanced rate. These *outward* propagating sound waves ultimately steepen into *forward* shocks. It is not quite clear at the moment whether the nonlinear growth of these waves saturates more quickly than the growth of inward propagating waves – so that reverse shocks still would dominate the wind structure –, or whether forward and reverse shocks possibly are of about equal strength in the fully developed wind structure.

Finally, *diagnostic tools* to analyze the degree to which these hydrodynamical models can reproduce the observed variability features of hot star winds are currently being developed in the X-ray domain (Hillier et al. 1993; Pauldrach et al. 1994a,b; Cooper & Owocki 1994; Feldmeier et al., in prep.) and for UV and optical spectral lines (Puls et al. 1993b, 1994). Only by detailed comparison between observed and computed diagnostics can we learn which dynamical structures out of a variety of theoretically possible ones are actually realized in these winds.

Acknowledgements. I wish to thank Drs. S. Owocki, J. Puls, A. Pauldrach, R.-P. Kudritzki, A. Fullerton, L. Lucy, and G. Cooper for many interesting discussions. Special thanks go to C. Reile for many stimulating and helpful discussions on (numerical) hydrodynamics. J. Puls, A. Fullerton, and R.-P. Kudritzki are thanked for carefully reading the manuscript. This work was supported by the DFG in the "Gerhard-Hess-Programm" under contract Pa 477/1-1. The calculations were performed on a Cray Y-MP at the Leibniz-Rechenzentrum in München.

Appendix A: estimate of the cooling length

The radiative cooling function in the form defined by Chevalier & Imamura (1982; CI) is,

$$\Lambda = \rho^2 A_{\rm CI} \left(\frac{p}{\rho}\right)^{\alpha} . \tag{A1}$$

Consider the flow problem of Sect. 4.1, where an ideal gas streams highly supersonically against a wall. The analytical solution for the stationary, plane-parallel cooling zone, assuming a cooling exponent $\alpha = -1/2$, is

$$\xi = \left(\frac{93\sqrt{3}}{320} - \frac{\pi}{8}\right)^{-1} \left\{ \frac{\sqrt{-w-w^2}}{20} \times (15 - 10w + 8w^2 - 464w^3 - 512w^4) - \frac{3}{8}\arccos(1+2w)\right\}, \tag{A2}$$

with the total cooling length,

$$L_{\rm c} = \frac{1}{32}\left(\frac{93\sqrt{3}}{320} - \frac{\pi}{8}\right) \frac{v_{\rm pre}^4}{A_{\rm CI}\,\rho_{\rm pre}}, \tag{A3}$$

and the total cooling time,

$$t_{\rm c} = \frac{5}{224} \frac{v_{\rm pre}^3}{A_{\rm CI}\,\rho_{\rm pre}} . \tag{A4}$$

Here, $\xi = x/L_{\rm c}$ is the normalized spatial variable, and $w = v/v_{\rm pre}$ is the normalized velocity. $\xi = 1$ is the position of the shock front, with $\xi = 0$ the location of the wall, where the cooled gas accretes in an infinitely thin, infinitely dense layer. $\rho_{\rm pre}$ and $v_{\rm pre}$ are the pre-shock density and velocity, respectively. We follow the convention of CI to take $v_{\rm pre}$ as a *positive* quantity, whereas the velocity v itself is a negative quantity; therefore, w is always negative.

To estimate the extent of the stationary cooling layer behind a stellar wind shock, we change from the above CI definition of the cooling function to the standard definition (cf. Raymond et al. 1976),

$$\Lambda = N_{\rm e} N_{\rm H} A_{\rm R}\, T^{\alpha}, \tag{A5}$$

so that

$$A_{\rm CI} = \frac{N_{\rm e} N_{\rm H}}{\rho^2} \left(\frac{\mu}{k}\right)^{\alpha} A_{\rm R} . \tag{A6}$$

Let $I_{\rm H}$ and $I_{\rm He}$ be the hydrogen and helium ionization degrees, and $Y = N_{\rm He}/N_{\rm H}$ be the helium fraction by number. Using (i) the strong shock jump conditions, (ii) the continuity equation for a stationary wind, (iii) a β-velocity law $v_{\rm stat} = v_\infty\,[1-(R_*/r)]^\beta$, and (iv) the fit (16), (17) to the cooling function, one finds from (A3) that

$$\frac{L_{\rm c}}{R_*} = 1.58\,10^{-17}\, C\, \frac{T_{\rm eff}^2 v_\infty R_*}{\dot{M}} \times \frac{r^2}{R_*^2}\left(1 - \frac{R_*}{r}\right)^{\beta} \frac{(T_{\rm post}/T_{\rm eff})^2}{\rho_{\rm pre}/\rho_{\rm stat}}, \tag{A7}$$

where a constant C of order unity has been introduced,

$$C = \frac{(1 + I_{\rm H} + Y(1 + I_{\rm He}))^{3/2}(1+4Y)^{1/2}}{I_{\rm H} + I_{\rm He}Y} . \tag{A8}$$

This can also be expressed in typical units for an O supergiant wind,

$$\frac{L_{\rm c}}{R_*} = 1.74\,10^{-10}\, C \left(\frac{T_{\rm eff}}{10\,000\,{\rm K}}\right)^2 \times \frac{v_\infty}{1\,000\,{\rm km\,s^{-1}}} \left(\frac{\dot{M}}{10^{-6} M_\odot {\rm yr}^{-1}}\right)^{-1} \frac{R_*}{R_\odot} \times \frac{r^2}{R_*^2}\left(1 - \frac{R_*}{r}\right)^{\beta} \frac{(T_{\rm post}/T_{\rm eff})^2}{\rho_{\rm pre}/\rho_{\rm stat}} . \tag{A9}$$

The *total* cooling length (A3) is now compared with the common estimate

$$L_{\rm c}^{1/{\rm e}} \approx -\frac{e}{\dot{e}}\, v_{\rm post}, \tag{A10}$$

where $\dot{e}$ is the energy loss due to radiative cooling. Using the strong shock conditions again, this leads to

$$L_{\rm c}^{1/e} = \frac{9\sqrt{3}}{2048}\,\frac{v_{\rm pre}^4}{A_{\rm CI}\,\rho_{\rm pre}}. \tag{A11}$$

This is a factor of 2.2 *larger* than the *total* cooling length (A3). The reason is that Field's (1965) thermal runaway is not included in the estimate (A10): the latter assumes "only" an exponentially growing cooling rate, whereas due to the runaway the slope in density and temperature at the end of the cooling zone is infinite.

Appendix B: radiative cooling within the viscous shock layer

The viscous layer of a strong shock has a thickness on the order of a particle mean free path. Competing with this is the length scale, over which radiative energy exchange plays a role, which is given by the usually much larger mean free path of a photon (cf. Zel'dovich & Raizer 1967, Sect. 14). Therefore, the viscous layer of a radiative shock (= shock front + cooling zone) is usually much narrower than the radiative cooling zone, over which the shock heated gas loses its thermal energy again. In contrast, for a *numerical* shock the viscous layer is smeared out over a few grid points by artificial viscosity, or by the numerical diffusivity of the scheme. It is therefore possible that the cooling layer becomes shorter than the viscous layer.

For a sufficiently small cooling exponent α (for the exact value see below) the material within this viscous layer, where $T < T_{\rm post}$, cools more efficiently than the post-shock material. If the cooling time within the shock front is shorter than the time it takes the particle to pass the front, severe numerical errors in the structure of the radiative shock will occur. Enhanced cooling within the viscous layer may therefore be the reason for the collapsed cooling zones in stellar wind simulations.

However, we show in this appendix: For a cooling exponent $\alpha = -1/2$, and for a post-shock cooling layer which is broader than the shock front, radiative cooling within the latter is of minor importance. Therefore, cooling zones which are principally resolved on the grid, i.e., are at least of the thickness of the viscous layer, are free of the numerical defect of enhanced cooling.

Let $\tau_{\rm c,vis}$ be the local cooling time for a fluid particle at a certain location within the viscous layer. (We use the abbreviation "vis" for quantities within this layer.) Let $\langle\tau_{\rm c,vis}\rangle$ be the cooling time of this particle, averaged over its trajectory through the front, and let $\tau_{\rm c,post}$ be the cooling time corresponding to the post-shock temperature. Finally, let $t_{\rm cross}$ be the time it takes the particle to cross the viscous layer. Then, if

$$\frac{\langle\tau_{\rm c,vis}\rangle}{t_{\rm cross}} = \kappa_{\rm c}\,\frac{\tau_{\rm c,post}}{t_{\rm cross}} \le F, \tag{B1}$$

where $\kappa_{\rm c} = \langle\tau_{\rm c,vis}\rangle/\tau_{\rm c,post}$, and F is a number of order unity, cooling within the shock front will influence the appearance of the radiative shock.

Mihalas & Mihalas (1984, p. 243), give the temperature stratification within the viscous layer,

$$\frac{T(v)}{T_{\rm pre}} = 1 + (\gamma - 1)\frac{v_{\rm h} - v}{v_{\rm h}} + \frac{1}{2}\gamma(\gamma - 1)\left(\frac{v_{\rm h} - v}{a_{\rm pre}}\right)^2, \tag{B2}$$

where $v_{\rm h}$ is the *upstream* velocity (i.e., the high velocity at the shock), and $a_{\rm pre}$ is the sound speed at the pre-shock side. For a strong shock and $\gamma = 5/3$, we have then (with $v_{\rm vis}$ the velocity *relative* to the shock front),

$$T = \frac{1}{3}\frac{\mu}{k}(v_{\rm h} - v)^2 = \frac{1}{3}\frac{\mu}{k}(v_{\rm pre} - v_{\rm vis})^2. \tag{B3}$$

Behind the shock, we have the well-known relation,

$$T_{\rm post} = \frac{1}{3}\frac{\mu}{k}v_{\rm jump}^2. \tag{B4}$$

Since we allow for radiative cooling within the viscous layer, Eq. (B3), which was derived for a purely viscous layer, is only approximately valid.

The velocity run within the front is approximately linear. Therefore, the flow time for a particle through this layer (of thickness δ) is,

$$t_{\rm cross} = \int_0^\delta \frac{{\rm d}x}{v_{\rm vis}} = \int_0^\delta \frac{{\rm d}x}{v_{\rm pre}(1 - \frac{3}{4}\frac{x}{\delta})} = \frac{\delta}{v_{\rm jump}}\ln 4. \tag{B5}$$

Here, $v_{\rm post} = \frac{1}{4}v_{\rm pre} = \frac{1}{3}v_{\rm jump}$ was used for a strong $\gamma = 5/3$ shock. $t_{\rm cross}$ is short compared with dynamical times, i.e., stationarity and plane-parallel geometry can be assumed,

$$\frac{\rho_{\rm vis}}{\rho_{\rm post}} = \frac{v_{\rm post}}{v_{\rm vis}}. \tag{B6}$$

The cooling time is of the order

$$\tau_{\rm c} \equiv -\frac{e}{\dot{e}} = \frac{3}{2}\frac{k}{\mu}\frac{T^{1-\alpha}}{A\,\rho}, \tag{B7}$$

hence the ratio of the local cooling time inside the front to the post-shock cooling time is given by

$$\frac{\tau_{\rm c,vis}}{\tau_{\rm c,post}} = \left(\frac{T_{\rm vis}}{T_{\rm post}}\right)^{1-\alpha}\frac{\rho_{\rm post}}{\rho_{\rm vis}}. \tag{B8}$$

Collecting these results together, one has

$$\begin{aligned}
\kappa_{\rm c} &= \frac{1}{t_{\rm cross}}\int_0^{t_{\rm cross}} \frac{\tau_{\rm c,vis}(t)}{\tau_{\rm c,post}}\,dt \\
&= \frac{1}{t_{\rm cross}}\int_0^{\delta}\left(\frac{v_{\rm pre} - v_{\rm vis}}{v_{\rm jump}}\right)^{2-2\alpha}\frac{v_{\rm vis}}{v_{\rm post}}\,\frac{{\rm d}x}{v_{\rm vis}} \\
&= \frac{3}{\ln 4}\,\frac{1}{3 - 2\alpha}.
\end{aligned} \tag{B9}$$

Here, it has been assumed that $\alpha < 3/2$: for larger values of α the integral diverges since the average cooling time inside

1995A&A...299..523F

the shock goes to ∞. From (B9) it follows that only for $\alpha < \frac{3}{2}(1 - \frac{1}{\ln 4}) \approx 0.418$ is $\kappa_c < 1$: Only for these values of α the averaged cooling time within the front is shorter than the post-shock cooling time.

For a cooling exponent $\alpha = -1/2$ one has from (B9),

$$\kappa_c \approx 0.541, \tag{B10}$$

i.e., $\alpha = -1/2$ is still not critical for enhanced cooling within the shock front, since the cooling time is on average only a factor of ≈ 0.541 shorter than the post-shock cooling time.

From (B1) one has, again using $\alpha = -1/2$, that cooling inside the viscous layer may modify the structure of the whole radiative shock only for

$$\tau_{\rm c,post} \le 2.56\, F\, \frac{\delta}{v_{\rm jump}} \tag{B11}$$

The post-shock cooling length is of the order

$$L_{\rm c,post} = \tau_{\rm c,post} \cdot v_{\rm post}, \tag{B12}$$

therefore only shocks with a radiative cooling zone of extent

$$\frac{L_{\rm c,post}}{\delta} \le 0.86\, F \tag{B13}$$

can be influenced by this defect. Since $F \approx 1$, this is no limitation at all. Radiative cooling within the viscous layer is therefore of no importance for those cooling zones which are principally resolved on the numerical grid.

Appendix C: resolution of the dense, cold domain of a radiative shock

Within a radiative cooling zone, Field's (1965) local thermal instability will generally occur: The subsonic post-shock domain is nearly isobaric (pressure differences will be compensated by sound waves), so that *cooling* leads to a *compression* of the gas. For isobaric cooling and a cooling exponent $\alpha < 2$ (Field 1965), material cools more efficiently at lower temperatures. This implies a *cooling runaway*, which shows up in the stationary CI-solutions for the radiative cooling zones in the infinite density and temperature gradients at the very end of the cooling zone (termed "ce", *cold edge*, in the following). This appendix deals with the numerical resolution of the infinite gradients at the "cold edge". For this, we demand the density to change from one grid point to the next by at most a factor of $F = O(1 \ldots 10)$. If i denotes the grid index, this implies

$$\frac{\rho_{i+1} - \rho_i}{\rho_i}\Big|_{\rm ce} \approx \frac{\rho'_i \cdot (x_{i+1} - x_i)}{\rho_i}\Big|_{\rm ce} \le F, \tag{C1}$$

The flow within the cooling zone is assumed to be stationary and plane-parallel, $\mathrm{d}_x(\rho v) = 0$, hence $(\rho'/\rho)|_{\rm ce} = (v'/v)|_{\rm ce}$ (a minus sign has been dropped which is of no significance in the following). With the normalized variables w and ξ from appendix A, the velocity gradient is given by

$$\frac{\mathrm{d}v}{\mathrm{d}x} = \frac{\mathrm{d}(w v_{\rm pre})}{\mathrm{d}(\xi L_{\rm c})} = \frac{v_{\rm pre}}{L_{\rm c}} \left(\frac{\mathrm{d}\xi}{\mathrm{d}w}\right)^{-1}, \tag{C2}$$

The differential $\mathrm{d}\xi/\mathrm{d}w$ can be calculated from Eq. (A2). Since, for strong shocks, $w_{\rm ce} \to 0$, only the lowest order in w is kept. From (A2) it is

$$\frac{\mathrm{d}\xi}{\mathrm{d}w}\Big|_{w\to 0} = 722.82\, w^{2-\alpha}. \tag{C3}$$

Furthermore,

$$\Delta x_{\rm ce} \le \frac{F \rho_{\rm ce}}{\rho'_{\rm ce}} = \frac{F v_{\rm ce}}{v'_{\rm ce}} = \frac{F v_{\rm ce} L_{\rm c}}{v_{\rm pre}} \frac{\mathrm{d}\xi}{\mathrm{d}w}\Big|_{\rm ce}. \tag{C4}$$

The radiative shock can be considered as an *isothermal* jump. Using the corresponding jump conditions ($\mathrm{Ma}_{\rm iso}$ being the isothermal Mach number), we have

$$\frac{\rho_{\rm ce}}{\rho_{\rm pre}} = \mathrm{Ma}_{\rm iso}^2 = \frac{v_{\rm pre}}{v_{\rm ce}} = w_{\rm ce}^{-1}, \tag{C5}$$

and therefore

$$\Delta x_{\rm ce} \le \frac{F L_{\rm c} C}{\mathrm{Ma}_{\rm iso}^{6-2\alpha}}. \tag{C6}$$

This is the expression for the grid resolution necessary to resolve the cold edge of the radiative shock.

Assuming $F = 10$, $\alpha = -1/2$, an equidistant spatial grid from 1 to 10 stellar radii, and a shock with cooling length $L_{\rm c} = 0.1\, R_*$ and Mach number $\mathrm{Ma}_{\rm iso} = 10$ (resp. 30), a total of $1.2\,10^5$ (resp. $2.7\,10^8$) grid points would then be needed to resolve the cold edge. These numbers are far beyond present computational capabilities. – In contrast, Fig. 5 shows a stationary cooling zone for $\alpha = 1$, $L_{\rm c} = 1$, $\mathrm{Ma}_{\rm iso} = \sqrt{20}$, where only 1 point per $L_{\rm c}$ should guarantee resolution. Instead, 50 grid points per $L_{\rm c}$ were used in this calculation.

We conclude that in wind calculations it is not possible to resolve the domain of steep gradients that define the end of the radiative cooling zones. This is a further justification for modifying the cooling function at low temperatures to hinder the collapse of the cooling layer, since this low temperature domain cannot be handled correctly anyway. On the other hand, a *conservative* numerical scheme always guarantees the correct total *jumps* in the hydrodynamical quantities across a radiative shock.

References

Abbott D.C., 1980, ApJ 242, 1183
Abbott D.C., 1982, ApJ 259, 282
Abbott D.C., Bieging J.H., Churchwell E., 1981, ApJ 250, 645
Abbott D.C., Telesco C.M., Wolff S.C., 1984a, ApJ 279, 225
Abbott D.C., Bieging J.H., Churchwell E., 1984b, ApJ 280, 671
Baade D., 1991, in: Baade D. (ed.) ESO Conference Proc. 36, Rapid Variability of OB-Stars. ESO, Garching, p. 217
Baade D., Lucy L.B., 1987, A&A 178, 213
Berger M.J., Colella P., 1989, J. Comp. Phys. 82, 64
Berger M.J., Oliger J., 1984, J. Comp. Phys. 53, 484
Bertschinger E., 1986, ApJ 304, 154
Bieging J.H., Abbott D.C., Churchwell E.B., 1989, ApJ 340, 518
Burgers J.M., 1950, Proc. Acad. Sci. Amst. 53, 732

Carlberg R.G., 1980, ApJ 241, 1131

Cassinelli J.P., Olson G.L., 1979, ApJ 229, 304

Cassinelli J.P., Swank J.H., 1983, ApJ 271, 681

Cassinelli J.P., Cohen D.H., MacFarlane J.J., Sanders W.T., Welsh B.Y., 1994, ApJ 421, 705

Castor J.I., Abbott D.C., Klein R.I., 1975, ApJ 195, 157

Chandrasekhar S., 1961, Hydrodynamic and Hydromagnetic Stability. Oxford Univ. Press, Oxford

Chevalier R.A., Imamura J.N., 1982, ApJ 261, 543 (CI)

Chlebowski T., 1989, ApJ 342, 1091

Chlebowski T., Harnden F.R., Sciortino S., 1989, ApJ 341, 427

Colella P., Woodward P.R., 1984, J. Comp. Phys. 54, 174

Cooper R.G., 1994, PhD thesis, University of Delaware

Cooper R.G., Owocki S.P., 1992, in: Drissen L., Leitherer C., Nota A. (eds.) ASP Conference Series 22, Nonisotropic and Variable Outflows from Stars. ASP, San Francisco, p. 281

Cooper R.G., Owocki S.P., 1994, in: Moffat A.F.J., Fullerton A.W., Owocki S.P., St-Louis N. (eds.) Instability and Variability of Hot Star Winds. Kluwer, Dordrecht (in press)

Courant R., Friedrichs K.O., 1948, Supersonic Flow and Shock Waves. Interscience Publishers, New York

Courant R., Friedrichs K.O., Lewy H., 1928, Math. Annalen 100, 32

Drew J.E., Denby M., Hoare M.G., 1994, MNRAS 266, 917

Ebbets D., 1982, ApJS 48, 399

Falle S.A.E.G., 1975, MNRAS 172, 55

Falle S.A.E.G., 1981, MNRAS 195, 1011

Feldmeier A., 1993, PhD thesis, Universität München

Feldmeier A., 1994, in: Moffat A.F.J., Fullerton A.W., Owocki S.P., St-Louis N. (eds.) Instability and Variability of Hot Star Winds. Kluwer, Dordrecht (in press)

Field G.B., 1965, ApJ 142, 531

Friend D.B., Abbott D.C., 1986, ApJ 311, 701

Fullerton A.W., Gies D.R., Bolton C.T., 1992, ApJ 390, 650

Gaetz T.J., Edgar R.J., Chevalier R.A., 1988, ApJ 329, 927

Gautschy A., Glatzel W., 1990, MNRAS 245, 597

Gies D.R., 1991, in: Baade D. (ed.) ESO Conference Proc. 36, Rapid Variability of OB-Stars. ESO, Garching, p. 229

Harnden F.R., Branduardi G., Elvis M., et al., 1979, ApJ 234, L51

Hawley J.F., Smarr L.L., Wilson J.R., 1984, ApJS 55, 211

Hearn A.G., 1972, A&A 19, 417

Hearn A.G., 1975, A&A 40, 277

Hedstrom G.W., 1979, J. Comp. Phys. 30, 222

Henrichs H.F., 1988, in: Conti P.S., Underhill A.B. (eds.) O Stars and Wolf-Rayet Stars. NASA, Washington, p. 199

Henrichs H.F., 1991, in: Baade D. (ed.) ESO Conference Proc. 36, Rapid Variability of OB-Stars. ESO, Garching, p. 199

Hillier D.J., Kudritzki R.P., Pauldrach A.W., et al., 1993, A&A 276, 117

Imamura J.N., Wolff M.T., Durisen R.H., 1984, ApJ 276, 667

Kaper L., 1993, PhD thesis, Sterrenkundig Instituut Amsterdam

Kaufer A., Stahl O., Wolf B., 1994, AG Abstract Series 10, 41

Kiriakidis M., Fricke K.J., Glatzel W., 1993, MNRAS 264, 50

Kudritzki R.P., Simon K.P., Hamann W.R., 1983, A&A 118, 245

Lamb H., 1945, Hydrodynamics. Dover reprint, New York

Lamers H.J.G.L.M., Waters L.B.F.M., 1984, A&A 138, 25

Landau L.D., Lifschitz E.M., 1991, Hydrodynamik. Akademie-Verlag, Berlin

Langer S.H., Chanmugam G., Shaviv G., 1981, ApJ 245, L23

Langer S.H., Chanmugam G., Shaviv G., 1982, ApJ 258, 289

Lucy L.B., 1982a, ApJ 255, 278

Lucy L.B., 1982b, ApJ 255, 286

Lucy L.B., 1983, ApJ 274, 372

Lucy L.B., 1984, ApJ 284, 351

Lucy L.B., Solomon P.M., 1970, ApJ 159, 879

Lucy L.B., White R.L., 1980, ApJ 241, 300

MacFarlane J.J., Cassinelli J.P., 1989, ApJ 347, 1090

MacGregor K.B., Hartmann L., Raymond J.C., 1979, ApJ 231, 514

Mair G., Müller E., Hillebrandt W., Arnold C.N., 1988, A&A 199, 114

Mihalas D., Mihalas B.W., 1984, Foundations of Radiation Hydrodynamics. Freeman, San Francisco

Milne E.A., 1926, MNRAS 86, 459

Moffat A.F.J., 1994a, in: Klare G. (ed.) Reviews in Modern Astronomy 7. Astronomische Gesellschaft, Hamburg, p. 51

Moffat A.F.J., 1994b, in: Moffat A.F.J., Fullerton A.W., Owocki S.P., St-Louis N. (eds.) Instability and Variability of Hot Star Winds. Kluwer, Dordrecht (in press)

Mullan D.J., 1984, ApJ 283, 303

Mullan D.J., 1986, A&A 165, 157

Noh W.F., 1987, J. Comp. Phys. 72, 78

Norman M.L., Winkler K.-H.A., 1986, in: Winkler K.-H.A., Norman M.L. (eds.) Astrophysical Radiation Hydrodynamics. Reidel, Dordrecht, p. 187

Norman M.L., Wilson J.R., Barton R.T., 1980, ApJ 239, 968

Owocki S.P., 1991, in: Crivellari L., Hubeny I., Hummer D.G. (eds.) Stellar Atmospheres, Beyond Classical Models. Kluwer, Dordrecht, p. 235

Owocki S.P., 1992, in: Heber U., Jeffery S. (eds.) The Atmospheres of Early-Type Stars. Springer-Verlag, Heidelberg, p. 393

Owocki S.P., 1994, in: Moffat A.F.J., Fullerton A.W., Owocki S.P., St-Louis N. (eds.) Instability and Variability of Hot Star Winds. Kluwer, Dordrecht (in press)

Owocki S.P., 1995, ApJ (preprint)

Owocki S.P., Rybicki G.B., 1984, ApJ 284, 337 (OR)

Owocki S.P., Rybicki G.B., 1985, ApJ 299, 265

Owocki S.P., Castor J.I., Rybicki G.B., 1988, ApJ 335, 914 (OCR)

Pauldrach A., 1987, A&A 183, 295

Pauldrach A., Puls J., Kudritzki R.P., 1986, A&A 164, 86

Pauldrach A.W.A., Kudritzki R.P., Puls J., Butler K., Hunsinger J., 1994a, A&A 283, 525

Pauldrach A.W.A., Feldmeier A., Puls J., Kudritzki R.P., 1994b, in: Vanbeveren D., van Rensbergen W., de Loore C. (eds.) Evolution of Massive Stars. Kluwer, Dordrecht, p. 105

Prinja R.K., 1988, MNRAS 231, 21p

Prinja R.K., Fullerton A.W., 1994a, ApJ 426, 345

Prinja R.K., Fullerton A.W., 1994b, in: Moffat A.F.J., Fullerton A.W., Owocki S.P., St-Louis N. (eds.) Instability and Variability of Hot Star Winds. Kluwer, Dordrecht (in press)

Prinja R.K., Howarth I.D., 1986, ApJS 61, 357

Prinja R.K., Howarth I.D., 1988, MNRAS 233, 123

Puls J., 1987, A&A 184, 227

Puls J., 1993, Habilitation, Universität München

Puls J., Pauldrach A.W.A., Kudritzki R.P., Owocki S.P., Najarro F., 1993a, in: Klare G. (ed.) Reviews in Modern Astronomy 6. Astronomische Gesellschaft, Hamburg, p. 271

Puls J., Owocki S.P., Fullerton A.W., 1993b, A&A 279, 457

Puls J., Feldmeier A., Springmann U., Owocki S.P., Fullerton A.W., 1994, in: Moffat A.F.J., Fullerton A.W., Owocki S.P., St-Louis N. (eds.) Instability and Variability of Hot Star Winds. Kluwer, Dordrecht (in press)

Puls J., Kudritzki R.P., Pauldrach A.W.A., et al., 1995, A&A (preprint)

Raymond J.C., Cox D.P., Smith B.W., 1976, ApJ 204, 290

Reile C., Gehren T., 1991a, A&A 242, 142

Reile C., Gehren T., 1991b, in: Crivellari L., Hubeny I., Hummer D.G. (eds.) Stellar Atmospheres, Beyond Classical Models. Kluwer, Dordrecht, p. 303

Roache P.J., 1982, Computational Fluid Dynamics. Hermosa Publishers, New Mexico

Rosner R., Tucker W.H., Vaiana G.S., 1978, ApJ 220, 643

Różyczka M., 1985, A&A 143, 59

Rybicki G.B., 1987, in: Lamers H.J.G.L.M., de Loore C.W.H. (eds.) Instabilities in Luminous Early Type Stars. Reidel, Dordrecht, p. 175

Rybicki G.B., Hummer D.G., 1978, ApJ 219, 654

Rybicki G.B., Owocki S.P., Castor J.I., 1990, ApJ 349, 274

Schulz W.D., 1964, J. Math. Phys. 5, 133

Schuster H.G., 1989, Deterministic Chaos. VCH Verlagsgesellschaft, Weinheim

Seward F.D., Forman W.R., Giacconi R., et al., 1979, ApJ 234, L55

Stone J.M., Norman M.L., 1992, ApJS 80, 753

Sturrock P.A., Spreiter J.R., 1965, J. Geophys. Res. 70, 5345

Tatsumi T., Tokunaga H., 1974, J. Fluid Mech. 65, 581

Thompson K.W., 1987, J. Comp. Phys. 68, 1

Thompson K.W., 1990, J. Comp. Phys. 89, 439

Van Leer B., 1977, J. Comp. Phys. 23, 276

Waldron W.L., Klein L., Altner B., 1992, in: Drissen L., Leitherer C., Nota A. (eds.) ASP Conference Series 22, Nonisotropic and Variable Outflows from Stars. ASP, San Francisco, p. 181

Waldron W.L., Klein L., Altner B., 1994, ApJ 426, 725

White R.L., 1985, ApJ 289, 698

White R.L., 1994, in: Moffat A.F.J., Fullerton A.W., Owocki S.P., St-Louis N. (eds.) Instability and Variability of Hot Star Winds. Kluwer, Dordrecht (in press)

White R.L., Chen W., 1992a, ApJ 387, L81

White R.L., Chen W., 1992b, in: Drissen L., Leitherer C., Nota A. (eds.) ASP Conference Series 22, Nonisotropic and Variable Outflows from Stars. ASP, San Francisco, p. 274

Winkler K.-H.A., Norman M.L., 1986, in: Winkler K.-H.A., Norman M.L. (eds.) Astrophysical Radiation Hydrodynamics. Reidel, Dordrecht, p. 71

Wolf B., Kaufer A., Rivinius T., Stahl O., 1994, AG Abstract Series 10, 40

Wu K., Chanmugam G., Shaviv G., 1992, ApJ 397, 232

Zel'dovich Ya.B., Raizer Yu.P., 1967, Physics of Shock Waves and High-Temperature Hydrodynamic Phenomena, Vol. II. Academic Press, New York

This article was processed by the author using Springer-Verlag LaTeX A&A style file *L-AA* version 3.